

The X-Shaped Milky Way Bulge in OGLE-III* Photometry and in N-Body Models

David M. Nataf¹†, Andrzej Udalski², Jan Skowron², Michał K. Szymański², Marcin Kubiak², Grzegorz Pietrzyński^{2,3}, Igor Soszyński², Krzysztof Ulaczyk², Łukasz Wyrzykowski^{2,4}, Radosław Poleski^{5,2}, E. Athanassoula⁶, Melissa Ness⁷, Juntai Shen⁸, Zhao-Yu Li⁸

¹Research School of Astronomy and Astrophysics, Australian National University, Canberra, ACT 2611, Australia

²Warsaw University Observatory, Al. Ujazdowskie 4, 00-478 Warszawa, Poland

³Universidad de Concepción, Departamento de Astronomía, Casilla 160-C, Concepción, Chile

⁴Institute of Astronomy, University of Cambridge, Madingley Road, Cambridge CB3 0HA, UK

⁵Department of Astronomy, Ohio State University, 140 W. 18th Ave., Columbus, OH 43210

⁶Aix Marseille Université, CNRS, LAM (Laboratoire d'Astrophysique de Marseille) UMR 7326, 13388, Marseille, France

⁷Max-Planck-Institut für Astronomie, Königstuhl 17, 69117 Heidelberg, Germany

⁸Key Laboratory for Research in Galaxies and Cosmology, Shanghai Astronomical Observatory, Chinese Academy of Sciences, 80 Nandan Road, Shanghai 200030, China

Accepted Received ; in original form.....

ABSTRACT

We model the split red clump of the Galactic bulge in OGLE-III photometry, and compare the results to predictions from two N-body models. Our analysis yields precise maps of the brightness of the two red clumps, the fraction of stars in the more distant peak, and their combined surface density. We compare the observations to predictions from two N-body models previously used in the literature. Both models correctly predict several features as long as one assumes an angle $\alpha_{\text{Bar}} \approx 30^\circ$ between the Galactic bar's major axis and the line of sight to the Galactic centre. In particular that the fraction of stars in the faint red clump should decrease with increasing longitude. The biggest discrepancies between models and data are in the rate of decline of the combined surface density of red clump stars toward negative longitudes and of the brightness difference between the two red clumps toward positive longitudes, with neither discrepancy exceeding $\sim 25\%$ in amplitude. Our analysis of the red giant luminosity function also yields an estimate of the red giant branch bump parameters toward these high-latitude fields, and evidence for a high rate ($\sim 25\%$) of disk contamination in the bulge at the colour and magnitude of the red clump, with the disk contamination rate increasing toward sightlines further distant from the plane.

Key words: Galaxy: Bulge – Galaxy: structure – Galaxy: stellar content

1 INTRODUCTION

The red clump (RC) has been used to trace the spatial structure of the inner Galaxy since the work of Stanek et al. (1994), who found that the dereddened RC apparent magnitudes were brighter toward positive longitudes. Stanek et al. (1994), and subsequently and in supe-

rior detail, Stanek et al. (1997), thus argued for a bar-shaped structure for the Galactic bulge, with the nearer end of the bar oriented toward positive longitudes with a viewing angle $\alpha_{\text{Bar}} \approx 25^\circ$ between the bar's major axis and the line of sight between the Sun and the Galactic centre. The advent

* Based on observations obtained with the 1.3 m Warsaw telescope at the Las Campanas Observatory of the Carnegie Institution for Science.
† Email: david.nataf@anu.edu.au

¹ This paper discusses two parameters often denoted as “ α ”, hence the subscripts leading to the parameter names α_{Bar} and α_{Skew} . The former refers to the viewing angle to the Galactic bar, the latter is a parameter in the skew-Gaussian distributions used to model the number counts of red clump stars.

of larger data surveys inevitably necessitated a more refined geometrical model. Nataf et al. (2010), in their analysis of OGLE-III photometry (Szymański et al. 2011), found that the RC brightness distribution shifted from being single-peaked to double-peaked toward sight lines near the Galactic bulge minor axis, far from the plane, with the two peaks having equal or nearly equal ($V - I$) colour. Concurrently and independently, McWilliam & Zoccali (2010) also found a double RC in OGLE-II (Udalski et al. 2002) and 2MASS data (Skrutskie et al. 2006), which they argued was due to an X-shaped bulge.

The hypothesis that the bifurcation in the apparent magnitude distribution of the RC was due to an X-shaped bulge was confirmed by Ness et al. (2012), who compared ARGOS spectroscopic (Freeman et al. 2013) and photometric data to N-body models (Athanasoula 2003) and demonstrated a stunning degree of consistency between observations and theoretical predictions. Ness et al. (2012) found that the double RC had to extend from no less than $b = -5^\circ$ to $b = -10^\circ$, that the two RCs had a radial velocity offset of the same sign and comparable size as dynamical predictions from N-body models, and that this morphology characterised the kinematics of bulge stars with $[\text{Fe}/\text{H}] \gtrsim -0.5$, in other words the vast majority ($\gtrsim 90\%$) of bulge stars. Simultaneously and independently, Li & Shen (2012) showed that the split red clump was also predicted by an N-body model previously used to successfully match to Milky Way bulge radial velocity data (Shen et al. 2010). Similar and additional kinematic comparisons between N-body model predictions and observations have since been reported by Vásquez et al. (2013) and Gardner et al. (2014).

This dynamical phenomenon begs detailed characterisation. The orbits that form the X-shaped structure are due to dynamical instabilities (Athanasoula 2005; Li & Shen 2012). As the orbital trajectories contributing to this morphology intersect the plane in a very specific manner (Skokos et al. 2002; Patsis et al. 2002), empirical study of these orbits could potentially constrain the gravitational potential along the inner Galactic plane, a matter of fundamental astrophysics that is difficult to investigate due to factors such as crowding and interstellar extinction. We note that this feature can be probed over all six dimensions of kinematic phase space – Poleski et al. (2013) mapped the streaming motions of the split RC in both transverse directions, μ_b and μ_l , with both showing strong signals.

Though the discovery of the split-RC showed great promise to further understanding of Galactic dynamics, early efforts at precision characterisation of the double RC hit a wall due to the various sources of noise in the colour-magnitude diagram. This is no surprise, as there were several uncertainties that needed to be cleared up, which we argue to be the parameters of the red giant branch bump (RGBB), as well as the extinction. The RGBB is an excess in the red giant luminosity function that occurs as the hydrogen-burning shell nears the convective envelope (Cassisi & Salaris 1997). Nataf et al. (2010) showed that the double RC behaves in an erratic manner toward negative longitudes, which they argued could be due to degeneracies between the faint RC and the bright RGBB. Nataf et al. (2011) and Nataf et al. (2013a) proceeded to characterise the RGBB of the Galactic bulge, and demonstrated that its properties were not consistent with predictions from canonical stellar evolution models

and current understanding of the bulge stellar population. We have adapted that methodology to double-RC sightlines to measure the RGBB parameters toward the higher latitude fields investigated in this work. Meanwhile, the complex matter of the reddening toward the bulge was largely resolved by Gonzalez et al. (2012) and Nataf et al. (2013b), at least for the sightlines relevant to this investigation.

An impressive recent analysis is that of Wegg & Gerhard (2013), who mapped the bulge RC in K-band using *VVV* photometry (Saito et al. 2012). They mitigated the systematic errors mentioned above by independently measuring the reddening, and using the same RGBB parameters as Nataf et al. (2013b). Their analysis benefits from broad coverage in both longitude and latitude, a rigorous treatment of errors, and an innovative non-parametric means to infer the geometrical distribution of bulge stars from their observed brightness and star count distribution functions. They reported a best-fit value for the bar’s angle of $\alpha_{\text{Bar}} = (27 \pm 2)^\circ$, that the X-shape begins at a height of ~ 400 pc from the plane, and that the Milky Way has a sharp X-shape. In contrast, it is estimated that only $\sim 33\%$ of bars in galaxies of Hubble type $-2 \leq T \leq 1$ (de Vaucouleurs class $S0^0$ to Sa) contain an X-shaped structure (Laurikainen et al. 2014), respectively rising to $38 \pm 9\%$ and $(62 \pm 9)\%$ of early-type $T = 2, 3$ (de Vaucouleurs class Sab, Sb) galaxies (Laurikainen et al. 2013).

In this investigation, we empirically characterise the luminosity function of the stellar population toward these high-latitude sightlines, the RGBB parameters and the exponential slope of the underlying RGB luminosity function, which should be of use to future studies. We do this using *I*-band photometry, where systematic errors from stellar evolution and possible metallicity gradients are minimised (Salaris & Girardi 2002). We measure the photometric observables of the double-RC as a function of direction: the distance to the brighter RC, the brightness separation between the two RCs, the total surface density of RC stars on the sky, and the fraction of stars in the brighter RC. We compare these results to predictions from two N-body models previously used to model dynamical data of the inner Galaxy.

2 DATA

OGLE-III observations were taken with the 1.3 meter Warsaw Telescope, located at the Las Campanas Observatory. The camera has eight 2048x4096 detectors, with a scale of approximately $0.26''/\text{pixel}$ yielding a combined field of view $0.6^\circ \times 0.6^\circ$. We use observations from 39 of the 267 OGLE-III fields directed toward the Galactic bulge, where we select those for which the coordinates of the field centre satisfy $(-5.00^\circ \leq l_{\text{central}} \leq 4.00^\circ, |b_{\text{central}}| \geq 5.00^\circ)$, keeping only those stars located on CCD chips (every OGLE-III field is made of 8 CCD chips) whose own centres satisfy that criteria. We deredden every star in those fields with the interpolated OGLE-III reddening and extinction maps of Nataf et al. (2013b). Individual OGLE-III fields were selected as the investigative fields for our analysis as they were found to be a good compromise between the larger field sizes (and thus larger star counts) desirable for precise measurements, and the smaller field sizes desirable so as not to

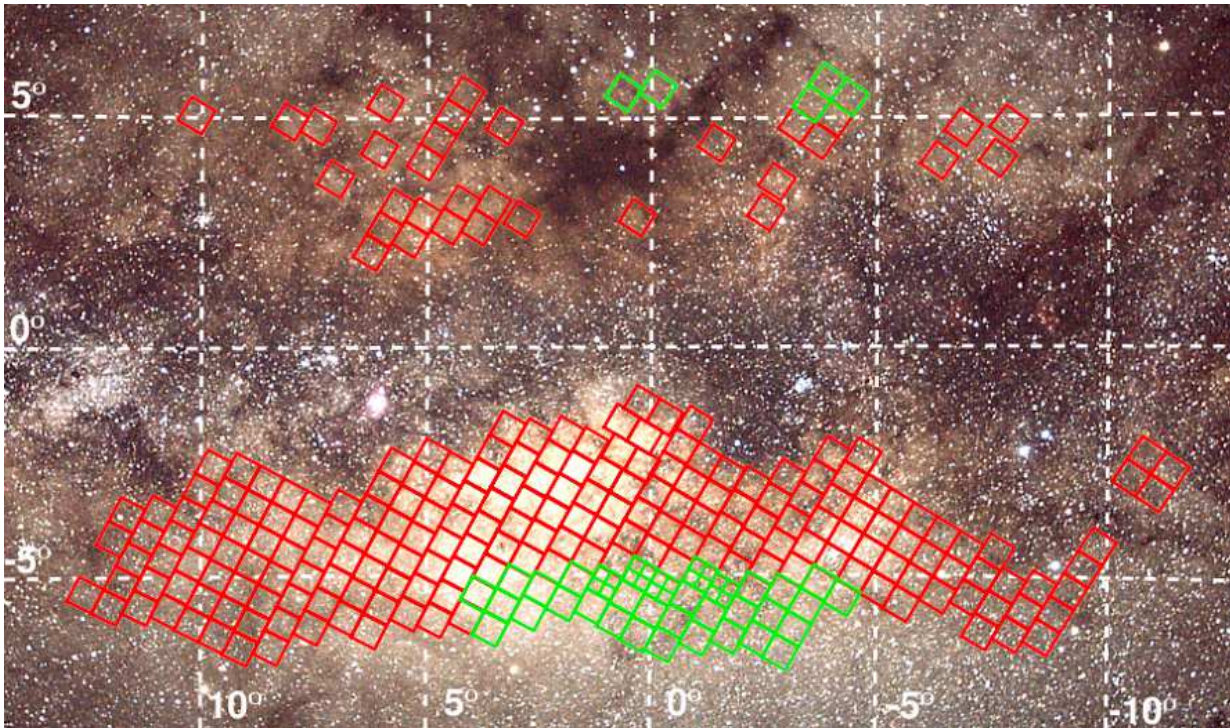


Figure 1. Coverage of the OGLE-III Galactic bulge photometric survey used in this work, overplotted on an optical image of the same area. Galactic coordinate system shown. The 54 OGLE-III calibration fields used in this work are shown as green squares, remaining fields are delineated by red squares.

smooth over gradients. For five OGLE-III fields (blg152, 159, 168, 176, and 186) for which coordinates of the field centres satisfy $(-1.75^\circ \leq l_{\text{central}} \leq 1.25^\circ, 5.00^\circ \leq |b_{\text{central}}| \leq 5.50^\circ)$, we split the OGLE-III field into four investigative fields (equivalent to two CCD chips), as the density of stars toward these sight lines is sufficiently high to allow a higher resolution in coordinate space, for a total of $34 + 20 = 54$ investigative fields, hereafter also referred to as calibration fields where appropriate. Our analysis is subsequently extended to 33 other OGLE-III fields toward larger longitudinal separations from the Galactic minor axis, for a total of 87 directions with measured parameters.

The photometric coverage used in this work is shown in Figure 1. More detailed descriptions of the instrumentation, photometric reductions and astrometric calibrations are available in Udalski (2003), Udalski et al. (2008) and Szymański et al. (2011). OGLE-III photometry and reddening maps are available for download from the OGLE webpage².

3 MEASURING THE PARAMETERS OF THE DOUBLE RED CLUMP

3.1 Overview of Fitting

Modelling and interpreting the distribution of stars toward sightlines with a double RC is a non-trivial task due to the large number of features in the colour-magnitude diagram

(CMD). There are two RCs, two RGBBs and two asymptotic giant branch bumps (AGBBs) mixed in with an underlying exponential-like luminosity function for the RGB and AGB stars, necessitating a diligent approach to avoid catastrophic degeneracies. All of these features are within our CMD selection box, which includes all stars redder than $(V - I) - (V - I)_{RC} \geq -0.30$ and $|I - I_{RC}| \leq 1.50$, where the mean values $(V - I)_{RC}, I_{RC}$ are as determined by Nataf et al. (2013b). We first attempted to model the luminosity function of the red giant branch using the same formalism as Nataf et al. (2013b), Poleski et al. (2013), and Wegg & Gerhard (2013) but we found that it was too costly to not fit for the skewness of the RCs. We have thus replaced the Gaussian distributions for the RCs with skew-Gaussian distributions, for which we fix the skew to be equal and opposite. Whereas a standard Gaussian distribution function is given by:

$$\phi(x) = \frac{1}{\sqrt{2\pi}} \exp\left[-\frac{x^2}{2}\right], \quad (1)$$

a skew-Gaussian is given by:

$$f(x) = 2\phi(x) \int_{-\infty}^{\alpha \text{Skew} x} \phi(t) dt, \quad (2)$$

where location and scale can be added in using the transformation:

$$x \rightarrow \frac{x - \xi}{\omega}, \quad (3)$$

² <http://ogle.astrouw.edu.pl/>

leading us to adopt the notation $f(\omega, \xi, \alpha_{\text{Skew}})$ for the skew-Gaussian distributions, with parameters:

$$\delta = \frac{\alpha_{\text{Skew}}}{\sqrt{1 + \alpha_{\text{Skew}}^2}} \quad (4)$$

$$\text{Mean} = I_{\text{RC}} = \xi + \omega\delta\sqrt{\frac{2}{\pi}} \quad (5)$$

$$\text{Variance} = \sigma_{\text{RC}}^2 = \omega^2 \left(1 - \frac{2\delta^2}{\pi}\right) \quad (6)$$

$$\text{Skewness} = \frac{4 - \pi}{2} \frac{\left(\delta\sqrt{2/\pi}\right)^3}{\left(1 - 2\delta^2/\pi\right)^{3/2}} \quad (7)$$

In the case $\alpha_{\text{Skew}} = 0$, the skew-Gaussian distribution reduces to a standard Gaussian distribution, with parameters $(\mu, \sigma) = (\xi, \omega)$. Conversely, as α_{Skew} approaches $\pm\infty$, the skew-Gaussian distribution converges to a half-Gaussian distribution, with skew approaching $\gamma_1 = \pm\sqrt{2}(4 - \pi)/(\pi - 2)^2 \approx \pm 0.995$. A set of demonstrative skew-Gaussian distributions are plotted in Figure 2, including the $\alpha_{\text{Skew}} = 1.5$ case assumed by our analysis. We note that given the demonstrative values $\mu = 0$ and $\sigma = 1$ with $\alpha_{\text{Skew}} = 1.5$ will yield a mode of $x = 0.543$, a median of $x = 0.624$, a mean of $x = 0.664$, a standard deviation of 0.748 and a skewness of 0.300.

We parametrize the luminosity function as follows:

$$N(m) = \sum_{i=1}^{i=2} \left\{ A_i \exp \left[B_i (I - I_{\text{RC},i}) \right] + N_{\text{RC},i} f(\omega_i, \xi_i, \alpha_{\text{Skew},i}) + \frac{N_{\text{RGBB},i}}{\sqrt{2\pi}\sigma_{\text{RGBB}}} \exp \left[-\frac{(I - I_{\text{RGBB},i})^2}{2\sigma_{\text{RGBB}}^2} \right] + \frac{N_{\text{AGBB},i}}{\sqrt{2\pi}\sigma_{\text{AGBB}}} \exp \left[-\frac{(I - I_{\text{AGBB},i})^2}{2\sigma_{\text{AGBB}}^2} \right] \right\},$$

where the parameters are as defined by Nataf et al. (2013b).

We reduce the number of free parameters by imposing the following constraints:

(i) The two RGBs have the same exponential slope parameter B , and the same ratio $EW_{\text{RC}} = N_{\text{RC},i}/A_i$ (2 constraints).

(ii) The integral of the number of stars in the parametrized luminosity function is made equal to the number of stars observed in the color-magnitude selection box (1 constraint).

(iii) Both AGBBs are fixed to have 2.8% the number of stars of their respective RCs, to be 1.07 mag brighter than their respective RCs, and to have the same magnitude dispersion as their respective RCs (6 constraints), as in Nataf et al. (2013b).

(iv) The skewness of the two RCs is equal and opposite, with the skewness of the brighter RC being strictly negative, i.e. a long tail toward brighter magnitudes (1 constraint). This is explored in Section 4.2.

There are 14 free parameters remaining following these constraints, which is still too large.

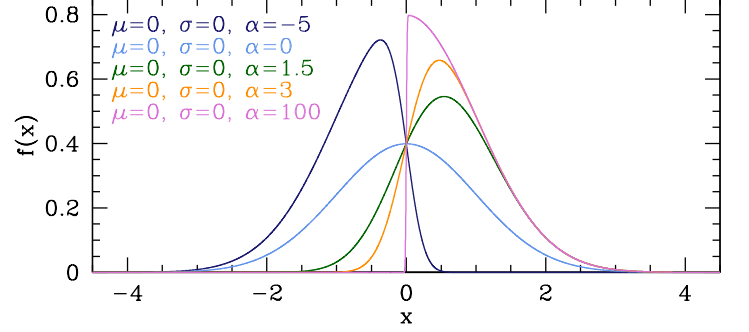


Figure 2. Skew-Gaussian distributions with $(\mu, \sigma) = (0, 1)$ plotted for demonstrative values of α , including the standard-normal case $\alpha = 0$, plotted in light blue. The $\alpha = 100$ case is visually indistinguishable from a half-Gaussian. Note that the parameters (μ, σ) are only equal to (ξ, ω) in the case $\alpha = 0$.

3.2 Further Constraints on the Red Giant Luminosity Function

We constrain the exponential slope of the RG luminosity function B , the mean value of the skewness parameter α_{Skew} , the ratio of the magnitude dispersion of the faint RC to that of the bright RC $\sigma_{\text{RC},2}/\sigma_{\text{RC},1}$, and the RGBB parameters $\Delta I_{\text{RGBB}}^{\text{RC}} = I_{\text{RGBB}} - I_{\text{RC}}$, $f_{\text{RGBB}}^{\text{RC}} = N_{\text{RGBB}}/N_{\text{RC}}$, and $\Delta\sigma^2 = \sigma_{\text{RGBB}}^2 - \sigma_{\text{RC}}^2$. The latter five parameters were iterated in a grid search, whereas B was allowed to float.

The best-fit values found for the fainter RC-RGBB pair are:

$$\Delta I_{\text{RGBB}}^{\text{RC}} = 0.610, \quad (8)$$

$$f_{\text{RGBB}}^{\text{RC}} = 0.160, \quad (9)$$

$$\Delta\sigma^2 = 0.0050, \quad (10)$$

$$\sigma_{\text{RC},2}/\sigma_{\text{RC},1} = 0.80, \quad (11)$$

$$\alpha_{\text{Skew}} = +1.50, \quad (12)$$

As stated before the two RCs have equal and opposite skew. For the brighter RC-RGBB pair, which is closer to the plane at fixed latitude and thus has a higher metallicity ($\Delta[\text{M}/\text{H}] \approx 0.06$ dex or $\Delta[\text{Fe}/\text{H}] \approx 0.08$ dex, Ness et al. 2013), we raise $\Delta I_{\text{RGBB}}^{\text{RC}}$ by 0.0535 mag and increase $f_{\text{RGBB}}^{\text{RC}}$ by 0.007, as per the empirical calibrations of Nataf et al. (2013b). We also fix the exponential parameter

$$B = 0.578, \quad (13)$$

which is both the mean and median value found, independently of the values of the other parameters. The combination of the six constraints on the RGBB, the constraint on B , and on the relative magnitude of the dispersion of the two RCs, leaves us with just five free parameters per field: $\sigma_{\text{RC},1}$, $I_{\text{RC},1}$, $I_{\text{RC},2}$, $N_{\text{RC},1}$, and $N_{\text{RC},2}$, though what we report is the brightness to the brighter RC, the brightness separation between the two RCs, the total surface density of RC stars on the sky, and the fraction of stars in the brighter RC.

Some of these constraints can be interpreted in a straightforward manner. The values of our RGBB parameters are consistent with a difference in the metallicity $\Delta[\text{M}/\text{H}] \approx 0.22$ dex (or $\Delta[\text{Fe}/\text{H}] \approx 0.27$ dex) between $(l, b) = (0^\circ, -2^\circ)$ (measured by Nataf et al. 2013b) and the sightlines investigated here, for which $(|l| \lesssim 3.5^\circ, 5^\circ \lesssim |b| \lesssim 7^\circ)$.

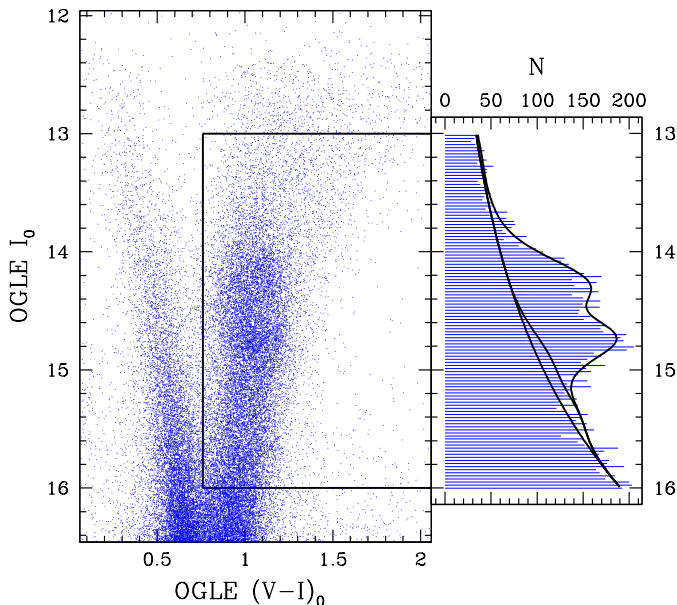


Figure 3. LEFT: Dereddened colour-magnitude diagram for the field BLG154, toward $(l, b) = (-1.04^\circ, -6.38^\circ)$. The colour-magnitude selection box is delineated by the thick, black rectangle. The bright red clump has a dereddened peak magnitude of $I_{RC,1} = 14.24 \pm 0.01$, and the magnitude difference between the two red clumps is $\Delta I = 0.52 \pm 0.01$. The fraction of stars in the faint red clump, $N_{\text{Faint}}/N_{\text{Total}}$, is $(43 \pm 2)\%$. RIGHT: Luminosity function for red giant and red clump stars.

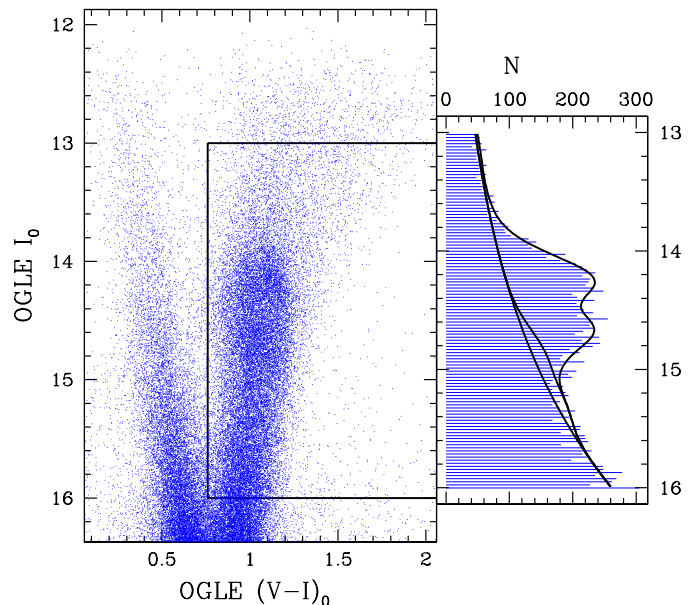


Figure 4. LEFT: Dereddened colour-magnitude diagram for the field BLG170, toward $(l, b) = (0.27^\circ, -6.31^\circ)$. The colour-magnitude selection box is delineated by the thick, black rectangle. The bright red clump has a dereddened peak magnitude of $I_{RC,1} = 14.19 \pm 0.01$, and the magnitude difference between the two red clumps is $\Delta I = 0.47 \pm 0.01$. The fraction of stars in the faint red clump, $N_{\text{Faint}}/N_{\text{Total}}$, is $(36 \pm 2)\%$. RIGHT: Luminosity function for red giant and red clump stars.

The dispersion for the fainter RC will be smaller than that of the brighter RC if the brightness dispersion is dominated by geometric dispersion, given that the fainter RC is further away. A distance modulus difference of $\delta\mu = 0.50$ mag yields $\sigma_{\mu,2}/\sigma_{\mu,1} \approx 10^{-0.1} = 0.79$. As this is consistent with the value found here of $\sigma_{RC,2}/\sigma_{RC,1} = 0.80 \pm 0.02$, it is likely that the observed magnitude dispersion of RC stars is dominated by geometric dispersion, and not by stellar evolution, photometric noise, or residual differential reddening. This constraint is explored in Section 4.2.

The clarity resulting from improved reddening maps and a more robust parameterization can be discerned in Figure 3, where we show the dereddened CMD for the OGLE-III field BLG154. The field contains 4006 ± 120 RC stars, yielding a convincing signal for not just the split-RC, but many of its features. We also plot the CMDs for BLG170 and BLG128 in Figure 4 and 5.

4 N-BODY MODELS

In order to facilitate interpretation of our data, we have convolved a scaled-solar, $t = 11$ Gyr, $[M/H] = +0.06$ theoretical RG+RC luminosity function from the BaSTI stellar database (Pietrinferni et al. 2004; Cordier et al. 2007)³ with two different N-body models, and then we applied our algorithms as described in Section 3.1 to see if we

can recover similar structural parameters. Our luminosity function assumes a Salpeter initial mass function (IMF) $dn/dm \propto m^{-2.35}$ (Salpeter 1955). In practice, the choice of IMF is predicted to have a negligible impact on RG luminosity functions, as evolution along the RG branch is fast (Bjork & Chaboyer 2006).

The two N-body models studied in this work have been selected as they have already been used in the bulge-related literature that has furthered understanding of Galactic dynamics.

We use the same N-body model as Ness et al. (2012), which consists of two live components, namely the halo and the disk, and is fully self-consistent. It was originally studied and developed by Athanassoula (2003) and described in those works. Ness et al. (2012) showed that the model includes a bimodal density peak along the line of sight, and approximately reproduces the sign and amplitude of the radial velocity differences between the two density peaks along the line of sight. At the time of the adopted snapshot, the corotation radius of the bar is ~ 6.3 Kpc and the circular velocity at that radius is ~ 210 km/s.

We also use the same N-body model as Shen et al. (2010), which was also studied by Li & Shen (2012), by Li et al. (2014) and by Shen (2014). The model of Shen et al. (2010) has been shown to match the directional-dependence of the first and second moments of the radial velocity distributions from the BRAVA survey (Kunder et al. 2012), to have an X-shaped bulge, and to have a radial velocity distribution function that is skew-symmetric for sightlines close to the plane. At the time of the adopted snapshot, the

³ BaSTI models can be found at the following URL: <http://basti.oa-teramo.inaf.it/index.html>

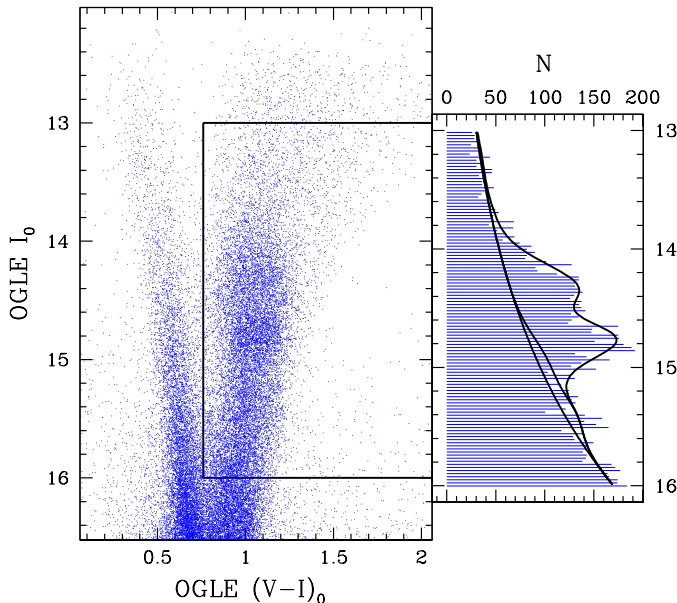


Figure 5. LEFT: Dereddened colour-magnitude diagram for the field BLG128, toward $(l, b) = (-2.90^\circ, -6.68^\circ)$. The colour-magnitude selection box is delineated by the thick, black rectangle. The bright red clump has a dereddened peak magnitude of $I_{RC,1} = 14.29 \pm 0.01$, and the magnitude difference between the two red clumps is $\Delta I = 0.50 \pm 0.01$. The fraction of stars in the faint red clump, $N_{\text{Faint}}/N_{\text{Total}}$, is $(49 \pm 2)\%$. RIGHT: Luminosity function for red giant and red clump stars.

corotation radius of the bar is ~ 4.5 Kpc and the circular velocity at that radius is ~ 180 km/s. A side-on view of the two models is shown in Figure 6.

Both models evolved from initial conditions with dynamically cold disks, such that Toomre’s $Q \approx 1.2$. In both cases, we adopt the same scale factors as assumed by those works in order for our comparisons to be consistent. We apply the 8-fold symmetry to both models to increase the effective star counts, and thus we only “observe” negative latitudes. We assume a distance to the Galactic Centre of $R_{GC} = 8.36$ Kpc from Chatzopoulos et al. (2014), who quoted an error of 0.11 Kpc. That measurement is based on a combined Bayesian analysis of the statistical parallax to the Milky Way’s old nuclear star cluster as well as the orbits of stars near Sgr A* from Gillessen et al. (2009). This distance is consistent with the recent estimate of $R_{GC} = (8.27 \pm 0.29)$ Kpc (Schönrich 2012), which is derived from solar neighbourhood kinematic data based on the assumption that the Milky Way disk is nearly axisymmetric.

The approach used here can best be discerned by inspecting Figure 7. We show a distance modulus distribution function for a sightline as predicted by the N-body models (top two panels), the absolute magnitude distribution function assumed (middle panel), and the final luminosity function that is the convolution of the intrinsic distance distribution and absolute magnitude distribution, with 0.05 mag of Gaussian noise added to simulate the effects of photometric errors, binaries, metallicity dispersion, and residual differential extinction (bottom panels). For these fits, we fix the AGBB and AGBB parameters to be the same as

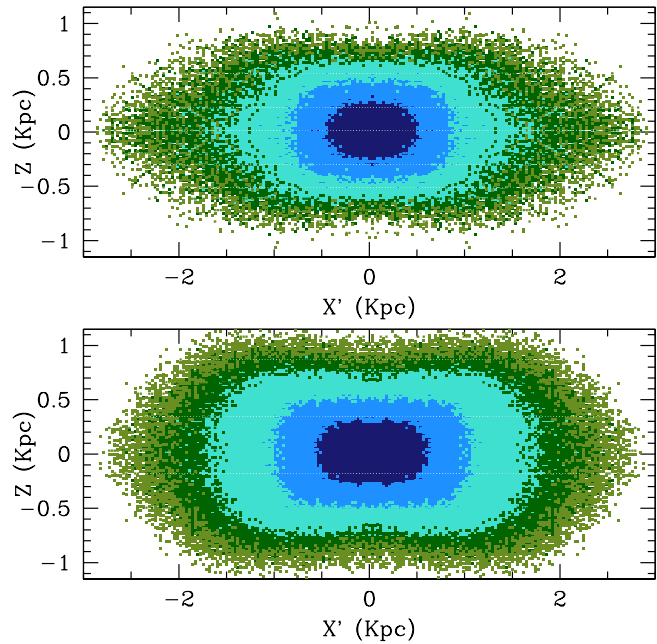


Figure 6. Density contours for the two N-body models used in this work, that of Ness et al. (2012) is shown in the top panel and that of Shen et al. (2010) is shown in the bottom-panel. Both models are viewed side-on, such that the major axis of the bar is perpendicular to the line of sight. The vertical axis is denoted $-Z$ and the planar axis parallel to the bar’s major axis is denoted X' . Colours denote the pixels containing 25%, 50%, 75%, 85% and 91% of the stars in these models within the coordinate range $\sqrt{(X'^2 + Y'^2)} \leq 3.0$ Kpc, $|Z| \leq 1.50$ Kpc, i.e. 25% of the stars in this coordinate range lie within the pixels drawn in dark blue points.

they are in the intrinsic luminosity function, the exponential slope parameter to $B = 0.60$ (Nataf et al. 2014). We fix $\sigma_{RC,2}/\sigma_{RC,1} = 0.80$, $\alpha_{\text{skew}} = +1.50$ for the faint RC, and $\alpha_{\text{skew}} = -1.50$ for the bright RC, as we did for the observations. Though it would be interesting to independently derive these parameters in the model, the number of stars in the models by Ness et al. (2012) and Shen et al. (2010) with $(|l| \lesssim 3.5^\circ, 5^\circ \lesssim |b| \lesssim 7^\circ)$ are $\sim 14,000$ and $\sim 78,000$ respectively, compared to $\sim 220,000$ RC+RGBB stars in the observations.

4.1 On the Selected Length Scale for the Models

The normalisation for distances (and velocities) in N-body models is arbitrary, and will depend on factors such as the assumed distance to the Galactic Centre, and the viewing angle to the Galactic bar. In particular, it will depend on which physical parameter is adopted to set the scale, as different parameters should yield different scale factors, since no N-body model is expected to be a perfectly scaled-replica of the Milky Way. Ness et al. (2012) scaled their N-body model by matching to the surface brightness maps from COBE (Dwek et al. 1995), and Shen et al. (2010) calibrated their length scales by matching their models to the radial velocity profile with direction measured by the BRAVA survey (Howard et al. 2008; Kunder et al. 2012).

Table 1. Comparison of distance scales between the data and the models.

Category	$I_{RC,\text{Faint}} - I_{RC,\text{Bright}}$ toward $(l, b) = (0^\circ, -5.5^\circ)$	$d \log \Sigma_{RC}/d b $ deg^{-1}	Scale Height (Kpc)
Data	0.48	-0.246	N/A
N2012 model, $\alpha_{\text{Bar}} = 30^\circ$	0.49	-0.284	0.254
S2010 model, $\alpha_{\text{Bar}} = 30^\circ$	0.50	-0.206	0.366

Table 2. Predicted skewness values and magnitude dispersions from the N-body models.

l	b	Skew ₁	Skew ₂	$\sigma_{RC,2}/\sigma_{RC,1}$	Skew ₁	Skew ₂	$\sigma_{RC,2}/\sigma_{RC,1}$
-	-	N2012	N2012	N2012	S2010	S2010	S2010
-3.00	-6.00	-0.91	0.66	0.78	-0.99	0.47	0.85
-2.00	-6.00	-0.90	0.55	0.78	-0.92	0.48	0.86
-1.00	-6.00	-0.81	0.52	0.79	-0.92	0.50	0.88
0.00	-6.00	-0.91	0.68	0.76	-0.93	0.45	0.89
1.00	-6.00	-0.92	0.49	0.83	-0.91	0.51	0.96
2.00	-6.00	-0.90	0.73	0.82	-0.98	0.52	0.98

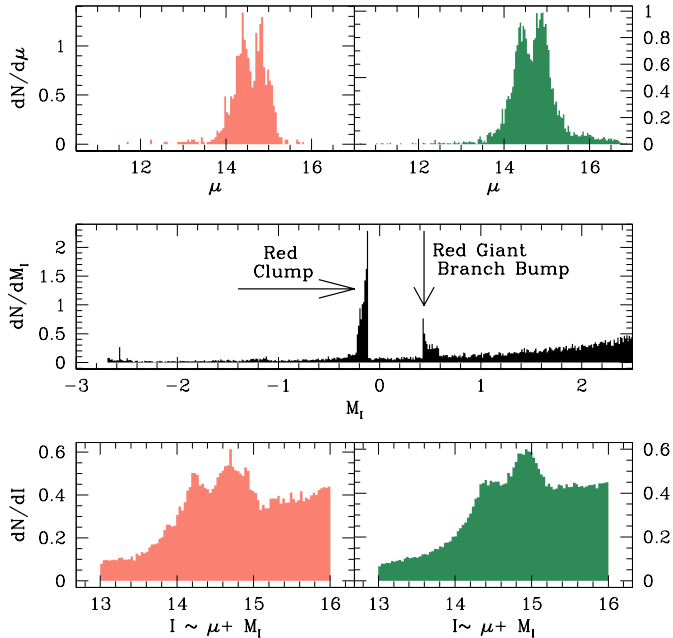


Figure 7. TOP: Predicted distance modulus distribution functions toward $(l, b) = (-1.00^\circ, -6.00^\circ)$ for the models of Ness et al. (2012) (Salmon) and Shen et al. (2010) (seagreen). MIDDLE: Scaled-solar, $t = 11$ Gyr, $[M/H] = +0.06$ theoretical RG+RC luminosity function from the BaSTI stellar database (Pietrinferni et al. 2004; Cordier et al. 2007) with which we convolve the N-body models. BOTTOM: Resultant apparent magnitude distribution function, where we have also added 0.05 mag of Gaussian noise to simulate the effects of secondary noise sources.

In Table 1, we show the relative distances achieved for two other observables we could have used to set the scale factors: the brightness separation between the bright and faint RC toward $(l, b) = (0^\circ, -5.5^\circ)$, and the observed latitudinal scale length of the surface density of RC stars, $d \log \Sigma_{RC}/d|b|$, toward $(-3.5^\circ \leq l \leq 2.5^\circ, 5.0^\circ \leq$

$|b| \leq 7.0^\circ)$. Impressively, the predicted brightness separation between the two peaks is a great match to the data for both models when the models oriented at an angle of $\alpha_{\text{Bar}} = 30^\circ$, which is consistent with the observational constraints (Cao et al. 2013; Wegg & Gerhard 2013).

We note that the observed value of $d \log \Sigma_{RC}/d|b|$ has a first-order mapping onto the exponential scale height, given by:

$$\frac{dZ}{d \log_e \Sigma} = \frac{\pi}{180} \frac{R_{GC}}{\log_e(10)} \left(\frac{d \log \Sigma}{d|b|} \right)^{-1} \approx 0.26 \text{ Kpc}. \quad (14)$$

This estimated scale height is marginally smaller than that of 0.27 Kpc reported by Cao et al. (2013). Comparison to the analysis of Wegg & Gerhard (2013) are more difficult as their scale height is position-dependent (though they determine a global-average scale height of 0.18 Kpc in their abstract). We restrict the comparison to their trend for the minor axis (the blue curve of their Figure 15), from which we estimate a scale height of ~ 0.33 Kpc. This is $\sim 27\%$ greater than the naive estimate of Equation 14.

However, if we repeat this calculation with one of our N-body models (Ness et al. 2012), given an average latitude of $|b| = 6^\circ$, $d \log \Sigma_{RC}/d|b| = -0.284$ (see the second row of Table 1), we obtain a scale height of ~ 223 pc. That answer may appear plausible, but it is not the true scale height. The actual scale height in the model of Ness et al. (2012) for $0.70 \leq Z/\text{Kpc} \leq 1.00$ and $\sqrt{X^2 + Y^2} \leq 3.0$ Kpc is 254 pc, a $\sim 14\%$ offset relative to the naive estimate. This discrepancy arises due to at least two reasons. First, the number density along the line of sight is bimodal, with the two peaks being at different heights for a given latitude. Second, within the models and plausibly within the Galaxy, scale height is a sensitive, non-linear function of Galactocentric radius, as such there will be some fuzziness when reporting any specific scale height.

4.2 On The Assumption of Equal and Opposite Skew and a Fixed Magnitude Dispersion Ratio

The availability of N-body models yields a means of verifying the reliability of three assumptions imposed in Section 3.2, that the two skews of the two RCs are equal and opposite, and that the ratio of their magnitude dispersions is fixed, such that $\sigma_{RC,2}/\sigma_{RC,1} = 0.80$ for all of our sightlines. It is non-trivial to precisely investigate this in the data as these parameters are strongly degenerate, both with each other but also with other parameters such as f_{RGBB}^{RC} and ΔI_{RGBB}^{RC} .

We model the skew by taking the distance modulus distribution functions for the N-body models, under the assumption that $\alpha_{\text{Bar}} = 30^\circ$, and convolve them with Gaussian noise of 0.05 mag. We partition the magnitudes into the ranges $13.61 < \mu_1 \leq 14.61$ and $14.61 < \mu_1 \leq 15.41$, where the dividing point of $\mu = 14.61$ is from our assumed distance to the Galactic centre of $R_{GC} = 8.36$ Kpc (Chatzopoulos et al. 2014), and is thus consistent with the position of the bifurcation, see the top panels of Figure 7. The results are listed in Table 2. We also experiment with other choices of limits and magnitude dispersion convolutions. What remains consistent are that the skews are both opposite in sign and large, $0.50 \leq \text{Skew} < 1.00$ (corresponding to $2 \lesssim \alpha_{\text{Skew}} < \infty$), and that $0.60 \lesssim \sigma_{RC,2}/\sigma_{RC,1} \lesssim 1.05$. The model of Shen et al. (2010) is better-fit by larger values of $\sigma_{RC,2}/\sigma_{RC,1}$ than that of Ness et al. (2012). That is likely due to the larger scale height of the bar in the model of Shen et al. (2010) (see Figure 6), which leads to a more populous faint RC relative to the bright RC.

Thus, the N-body model predictions are slightly offset from our best-fit values used in Section 3.2, and even further offset from the assumption of two Gaussians or even two Gaussians of equal magnitude dispersions ubiquitously assumed in the literature prior to this investigation. However, all of these assumptions are less offset from each other than they would be from the the severe, unphysical, degeneracy-induced variations that would be “measured” from one sightline to the next if no constraints were imposed. As the discrepancy may come from factors other than the geometry of the bar, for example undiagnosed sources of noise in the colour-magnitude diagram, or the greater incidence of disk contamination seen in the data relative to the models (see Section 5.4), we opt to leave our assumptions for these two parameters as they are. The outstanding uncertainty in these parameters suggests that measurements of bulk properties of the combined RCs such as EW_{RC} and Σ_{RC} are likely more reliable than those of relative properties between the two RCs, such as $N_{\text{Faint}}/N_{\text{Total}}$.

5 PHOTOMETRIC ANALYSIS OF THE DOUBLE RED CLUMP: RESULTS

Our key findings concern the brightness of the two RCs, the total surface density of RC stars deg^{-2} , Σ_{RC} , the fraction of RC stars in the faint RC, $N_{\text{Faint}}/N_{\text{Total}}$, and the ratio of RC stars to the number density of RG stars at the luminosity of the RC, EW_{RC} . We discuss each of these separately. Our results for our 54 calibration fields are enumerated in Table 3, with the results of the analysis extended to 33 other fields

and Table 4. The error values are 1- σ errors estimated via Markov Chain Monte Carlo, they are purely statistical and do not include the effects of systematic errors.

The parameters toward the field blg159A are clearly erroneous as they differ remarkably from those of neighbouring fields, which may be a product of unresolved differential reddening toward that field. We have verified that this field does not impact our selection of the best-fit RGBB parameters, or any of the other parameters and conclusions discussed later in this work.

Table 3. Parameters of split red clumps toward the 54 calibration fields, listed in order of increasing Galactic longitude. Listed are the OGLE-III field names, the field centres in Galactic coordinates, the dereddened apparent magnitude of the brighter red clump $I_{RC,1}$, the brightness difference between the two red clumps (ΔI), the fraction of red clump stars in the faint red clump ($N_{\text{Faint}}/N_{\text{Total}}$), the total number of red clump stars N_{RC} , the surface density of red clump stars per deg², the number density of red giant stars at the luminosity of the red clump EW_{RC} , and the magnitude dispersion of the brighter red clump, Σ_{RC} . Some OGLE-III fields are split into components {A,B,C,D}.

Field	l	b	$I_{RC,1}$	ΔI	$N_{\text{Faint}}/N_{\text{Total}}$	N_{RC}	Σ_{RC}	EW_{RC}	$\sigma_{RC,1}$
blg363	-4.37	5.43	14.36±0.02	0.38±0.02	0.54±0.04	7130± 167	20286± 475	1.08±0.04	0.23±0.01
blg120	-4.25	-5.50	14.35±0.01	0.39±0.01	0.50±0.02	6968± 138	19504± 386	1.10±0.03	0.20±0.01
blg360	-3.89	5.78	14.32±0.01	0.44±0.01	0.57±0.02	6236± 142	17306± 394	1.07±0.03	0.21±0.01
blg125	-3.75	-5.19	14.36±0.01	0.38±0.01	0.51±0.02	8855± 157	24156± 428	1.20±0.03	0.20±0.01
blg359	-3.56	5.31	14.43±0.02	0.39±0.01	0.49±0.03	8463± 165	23427± 458	1.18±0.03	0.22±0.01
blg126	-3.46	-5.69	14.34±0.01	0.42±0.01	0.55±0.02	6526± 137	17822± 374	1.08±0.03	0.20±0.01
blg127	-3.18	-6.18	14.25±0.01	0.47±0.01	0.55±0.02	4590± 121	13187± 346	1.00±0.04	0.20±0.01
blg135	-2.95	-5.38	14.30±0.01	0.43±0.01	0.55±0.01	8068± 155	21929± 420	1.14±0.03	0.20±0.01
blg128	-2.90	-6.68	14.29±0.01	0.50±0.01	0.49±0.02	3252± 107	9704± 319	0.90±0.04	0.20±0.01
blg136	-2.67	-5.89	14.28±0.02	0.46±0.01	0.51±0.02	6207± 148	16995± 406	1.09±0.04	0.23±0.01
blg137	-2.39	-6.39	14.25±0.01	0.49±0.01	0.51±0.01	4269± 118	11815± 326	0.96±0.03	0.20±0.01
blg144	-2.30	-5.34	14.30±0.05	0.45±0.10	0.40±0.11	8511± 281	23152± 765	1.25±0.05	0.27±0.02
blg145	-2.02	-5.84	14.21±0.01	0.48±0.01	0.49±0.02	5951± 136	16209± 371	1.08±0.03	0.22±0.01
blg152D	-1.81	-5.31	14.26±0.11	0.38±0.17	0.56±0.20	1885± 88	20556± 958	1.08±0.07	0.29±0.03
blg146	-1.74	-6.34	14.24±0.01	0.51±0.01	0.48±0.02	4171± 119	11742± 336	0.96±0.04	0.20±0.01
blg152A	-1.66	-5.57	14.21±0.03	0.43±0.02	0.51±0.05	1549± 70	16885± 765	0.96±0.06	0.22±0.02
blg152C	-1.54	-5.16	14.26±0.03	0.45±0.02	0.42±0.05	2100± 84	22881± 917	1.10±0.06	0.23±0.02
blg152B	-1.39	-5.42	14.26±0.08	0.48±0.10	0.45±0.13	1886± 125	20503± 1353	1.19±0.10	0.28±0.03
blg153	-1.32	-5.86	14.24±0.01	0.47±0.01	0.44±0.02	5516± 131	15125± 358	1.04±0.03	0.21±0.01
blg159D	-1.32	-4.96	14.27±0.03	0.50±0.02	0.44±0.04	2549± 100	27553± 1077	1.31±0.07	0.25±0.02
blg159A	-1.18	-5.22	14.37±0.02	0.73±0.07	0.13±0.03	2151± 116	23282± 1259	1.28±0.09	0.31±0.02
blg159C	-1.06	-4.81	14.27±0.02	0.45±0.02	0.44±0.03	2468± 85	26713± 919	1.15±0.06	0.22±0.01
blg154	-1.04	-6.38	14.24±0.01	0.52±0.01	0.43±0.02	4006± 120	11315± 338	1.04±0.04	0.22±0.01
blg159B	-0.91	-5.07	14.23±0.02	0.44±0.02	0.43±0.04	2143± 79	23148± 850	1.17±0.06	0.22±0.01
blg160	-0.84	-5.53	14.22±0.01	0.49±0.01	0.46±0.01	6672± 149	18187± 405	1.13±0.03	0.22±0.01
blg161	-0.56	-6.02	14.21±0.01	0.51±0.01	0.43±0.02	5569± 134	15189± 366	1.09±0.04	0.22±0.01
blg168D	-0.49	-5.24	14.25±0.02	0.50±0.02	0.39±0.03	2091± 81	22879± 886	1.25±0.07	0.23±0.01
blg168A	-0.34	-5.50	14.26±0.02	0.46±0.02	0.40±0.04	1576± 68	17199± 745	1.05±0.06	0.21±0.01
blg162	-0.29	-6.52	14.17±0.01	0.53±0.01	0.39±0.02	3419± 109	9710± 309	0.92±0.04	0.21±0.01
blg168C	-0.22	-5.09	14.22±0.05	0.45±0.09	0.38±0.12	2128± 81	23289± 882	1.20±0.06	0.25±0.03
blg357	-0.13	5.64	14.35±0.01	0.49±0.01	0.40±0.01	5933± 143	17152± 413	1.08±0.04	0.20±0.01
blg168B	-0.07	-5.35	14.24±0.02	0.44±0.02	0.41±0.03	1777± 74	19425± 805	1.12±0.06	0.20±0.02
blg169	-0.00	-5.80	14.23±0.01	0.49±0.01	0.39±0.02	6485± 145	18026± 404	1.21±0.04	0.22±0.01
blg176D	0.03	-4.95	14.22±0.02	0.45±0.02	0.43±0.03	2384± 82	25796± 891	1.25±0.06	0.22±0.01
blg176A	0.17	-5.21	14.23±0.02	0.45±0.02	0.43±0.03	2063± 80	22171± 856	1.16±0.06	0.21±0.01
blg170	0.27	-6.31	14.19±0.01	0.52±0.01	0.36±0.02	3981± 117	11522± 337	0.90±0.03	0.20±0.01
blg176C	0.29	-4.80	14.20±0.02	0.46±0.01	0.45±0.03	2578± 82	27762± 880	1.25±0.06	0.22±0.01
blg176B	0.44	-5.07	14.23±0.02	0.41±0.01	0.43±0.04	2122± 73	22830± 789	1.14±0.05	0.20±0.01
blg177	0.51	-5.51	14.23±0.01	0.47±0.01	0.39±0.01	7176± 146	19496± 396	1.13±0.03	0.20±0.01
blg355	0.62	5.57	14.31±0.01	0.49±0.01	0.39±0.02	6502± 158	18471± 448	1.12±0.04	0.22±0.01
blg178	0.78	-6.01	14.20±0.01	0.48±0.01	0.34±0.02	5229± 128	14455± 354	1.03±0.03	0.20±0.01
blg186D	0.81	-5.14	14.24±0.01	0.46±0.02	0.32±0.03	2143± 79	23201± 855	1.13±0.06	0.20±0.01
blg186A	0.95	-5.40	14.22±0.01	0.48±0.02	0.35±0.02	1886± 71	20401± 763	1.11±0.06	0.18±0.01
blg186C	1.08	-4.99	14.24±0.01	0.45±0.02	0.36±0.03	2416± 82	26159± 887	1.23±0.06	0.21±0.01
blg186B	1.22	-5.25	14.25±0.01	0.47±0.02	0.30±0.03	2253± 77	24284± 832	1.30±0.06	0.21±0.01
blg187	1.29	-5.69	14.21±0.01	0.46±0.01	0.34±0.02	5933± 134	16256± 368	1.04±0.03	0.20±0.01
blg192	1.65	-5.12	14.23±0.01	0.43±0.01	0.32±0.02	8579± 160	23301± 434	1.15±0.03	0.20±0.01
blg193	1.92	-5.62	14.21±0.01	0.45±0.01	0.32±0.02	6390± 138	17606± 382	1.09±0.03	0.20±0.01
blg199	2.44	-5.33	14.21±0.01	0.44±0.02	0.26±0.02	8183± 156	22176± 424	1.20±0.03	0.21±0.01
blg204	2.71	-5.84	14.15±0.01	0.46±0.01	0.27±0.02	6216± 140	17163± 386	1.16±0.03	0.21±0.01
blg211	3.03	-5.18	14.20±0.01	0.44±0.02	0.25±0.02	8144± 158	22394± 435	1.21±0.03	0.22±0.01
blg212	3.30	-5.68	14.18±0.02	0.45±0.03	0.21±0.04	6966± 147	18908± 399	1.22±0.03	0.24±0.01
blg213	3.57	-6.19	14.14±0.01	0.46±0.02	0.24±0.03	5216± 130	14633± 364	1.12±0.04	0.22±0.01
blg221	3.84	-5.42	14.14±0.01	0.39±0.02	0.26±0.04	7375± 147	20022± 399	1.17±0.03	0.21±0.01

Table 4. Parameters of split red clumps toward 33 additional fields not used for calibration. Definitions of the parameters and can be found in the caption to Table 3. The larger error values and decreased trends demonstrate that the split red clump is sharply falling off toward these fields, which are at larger longitudinal separation from the Galactic minor axis than the calibration fields.

Field	l	b	$I_{RC,1}$	ΔI	$N_{\text{Faint}}/N_{\text{Total}}$	N_{RC}	Σ_{RC}	EW_{RC}	$\sigma_{RC,1}$
blg327	-9.17	-5.29	14.54±0.19	0.48±0.17	0.19±0.25	1755± 110	5284± 331	0.53±0.04	0.24±0.04
blg328	-8.87	-5.79	14.24±0.19	0.46±0.17	0.80±0.24	1656± 116	4859± 341	0.52±0.05	0.32±0.04
blg329	-8.59	-6.27	14.46±0.02	0.36±0.02	0.43±0.04	862± 57	3769± 249	0.48±0.04	0.15±0.02
blg322	-8.57	-5.28	14.55±0.04	0.58±0.12	0.13±0.09	1900± 119	7564± 472	0.70±0.05	0.27±0.02
blg323	-8.41	-5.72	14.30±0.09	0.43±0.17	0.56±0.17	457± 42	6226± 571	0.65±0.08	0.20±0.04
blg324	-7.94	-6.24	14.59±0.07	0.00±0.17	0.00±0.14	2065± 124	6054± 364	0.68±0.05	0.31±0.04
blg319	-7.86	-5.21	14.57±0.04	0.67±0.12	0.09±0.10	3395± 193	9430± 535	0.78±0.05	0.29±0.02
blg320	-7.57	-5.71	14.54±0.06	0.79±0.17	0.05±0.15	3280± 181	9014± 497	0.85±0.05	0.30±0.03
blg321	-7.28	-6.19	14.55±0.06	0.80±0.17	0.05±0.13	2589± 161	7867± 489	0.81±0.06	0.30±0.03
blg318	-7.02	-5.46	14.50±0.05	0.41±0.17	0.22±0.21	3741± 155	10269± 425	0.82±0.04	0.25±0.04
blg315	-6.36	-5.42	14.37±0.03	0.38±0.02	0.52±0.04	4583± 128	12869± 358	0.93±0.03	0.21±0.01
blg110	-5.85	-5.12	14.40±0.03	0.37±0.02	0.48±0.07	6958± 160	18892± 433	1.06±0.03	0.22±0.02
blg111	-5.56	-5.61	14.33±0.02	0.41±0.02	0.57±0.03	4020± 109	15475± 421	1.07±0.04	0.22±0.01
blg115	-5.42	-5.22	13.90±0.12	0.79±0.10	0.74±0.06	157± 23	25301± 3707	1.37±0.30	0.30±0.05
blg336	4.50	5.06	14.24±0.11	0.71±0.11	0.08±0.08	4356± 61	23591± 331	1.30±0.02	0.28±0.01
blg230	4.54	-5.48	14.12±0.02	0.41±0.02	0.26±0.04	4646± 115	17021± 420	1.10±0.04	0.21±0.01
blg231	4.80	-5.98	14.13±0.02	0.41±0.03	0.25±0.05	5383± 131	15267± 372	1.12±0.04	0.22±0.01
blg239	5.13	-5.34	14.13±0.02	0.39±0.03	0.25±0.06	6430± 140	17661± 384	1.13±0.03	0.23±0.01
blg240	5.40	-5.84	14.17±0.13	0.10±0.13	0.50±0.22	3582± 106	14014± 415	1.04±0.04	0.32±0.03
blg246	5.59	-5.21	14.10±0.03	0.44±0.13	0.25±0.20	1835± 72	20361± 801	1.33±0.07	0.24±0.04
blg247	6.01	-5.72	14.11±0.02	0.43±0.02	0.30±0.04	5194± 125	14146± 340	1.12±0.04	0.22±0.01
blg248	6.28	-6.21	13.74±0.14	0.47±0.14	0.91±0.13	3601± 114	10667± 337	1.02±0.04	0.33±0.01
blg255	6.52	-5.42	14.00±0.08	0.41±0.09	0.48±0.16	5792± 144	15804± 393	1.19±0.04	0.29±0.02
blg256	6.79	-5.93	14.08±0.08	0.43±0.17	0.25±0.21	4298± 157	11930± 436	1.08±0.05	0.26±0.04
blg262	7.04	-5.11	14.00±0.02	0.46±0.01	0.42±0.04	5388± 134	14766± 367	1.14±0.04	0.25±0.02
blg263	7.30	-5.63	14.18±0.09	0.11±0.17	0.27±0.20	4863± 142	13210± 386	1.07±0.04	0.35±0.03
blg264	7.57	-6.13	14.17±0.08	0.79±0.14	0.03±0.20	3666± 111	10427± 314	1.10±0.04	0.30±0.04
blg268	7.66	-5.03	13.99±0.03	0.47±0.02	0.44±0.05	5269± 141	14474± 387	1.05±0.04	0.26±0.02
blg269	7.93	-5.55	13.99±0.06	0.40±0.17	0.46±0.14	3935± 118	10825± 325	0.90±0.03	0.25±0.02
blg270	8.19	-6.06	13.93±0.07	0.41±0.12	0.48±0.15	3240± 109	8957± 301	0.94±0.04	0.26±0.03
blg275	8.34	-5.05	13.98±0.05	0.47±0.03	0.38±0.09	4161± 130	12311± 384	1.00±0.04	0.28±0.02
blg271	8.47	-6.55	14.12±0.14	0.16±0.17	0.14±0.22	1679± 77	6995± 320	0.86±0.05	0.30±0.04
blg276	8.55	-5.59	14.03±0.10	0.47±0.17	0.22±0.21	1747± 107	9589± 586	0.90±0.06	0.28±0.04

5.1 The Brightness of the Two Red Clumps as a Function of Position

The apparent magnitude of the brighter RC is a decreasing function of increasing longitude and increasing separation from the plane:

$$\begin{aligned}
 I_{RC,1} &= (14.263 \pm 0.004) + (-0.022 \pm 0.001) \times (l) \\
 &\quad + (-0.042 \pm 0.004) \times (|b| - 5), \\
 \delta &= 0.0034, \\
 \chi^2 &= 78.22, \\
 \text{DoF} &= 43,
 \end{aligned} \tag{15}$$

where the fit (and all subsequent linear fits in this section) is computed using the standard formalism for weighted multi-linear least-squares fit, with the weights given by the inverse square of the errors on the measured values of the dependent variable (in this case $I_{RC,1}$), and 3.0σ outliers recursively removed. We also state the resultant scatter δ and χ^2 , as well as the degrees of freedom (DoF) of the fit, which is equal to

the difference between the number of non-outlier data points and the number of free parameters to the fit.

The brightness separation between the two RCs is a slowly and quadratically decreasing function of separation from the minor axis and a rapidly increasing function of separation from the plane:

$$\begin{aligned}
 \Delta I &= (0.449 \pm 0.004) + (-0.0049 \pm 0.0003) \times (l)^2 \\
 &\quad + (0.053 \pm 0.004) \times (|b| - 5), \\
 \delta &= 0.0025, \\
 \chi^2 &= 48.22, \\
 \text{DoF} &= 48.
 \end{aligned} \tag{16}$$

The latitudinal dependence clearly illustrates the fact that at larger separations from the plane, the arms of the X-shape move outward. If we extrapolate the fit to the origin, we obtain a brightness separation toward $(l, b) = (0^\circ, 0^\circ)$ of $\Delta I = 0.182 \pm 0.024$ – not consistent with zero. Our findings are therefore marginally suggestive of an open-X rather than a closed-X morphology for the Galactic bulge, in other words the extrapolations of the arms of the X-shape, were they to be viewed side on, would not intersect at the Galactic centre, see Bureau et al. (2006) and Patsis et al. (2002) for further discussion.

We show the projected positions of the RC centroids (assuming $M_{I,RC} = -0.12$, Nataf et al. 2013b) in Figure 8.

5.2 The Combined Surface Density of Red Clump Stars on the Sky

The combined surface density of bright and faint RC stars on the sky is a steeply declining function of separation from the plane:

$$\begin{aligned}
 \log_{10}(\Sigma_{RC}) &= (4.411 \pm 0.003) + (-0.246 \pm 0.004) \times (|b| - 5), \\
 \delta &= 0.0035, \\
 \chi^2 &= 97.28, \\
 \text{DoF} &= 36.
 \end{aligned} \tag{17}$$

This can also be discerned in Figure 9, where we show the scatter of surface density as a function of absolute latitude. The surface density - latitude relation is strikingly consistent with an exponential density profile for the Galactic bulge.

5.3 The Fraction of Red Clump Stars in the Faint Red Clump

The best-fit relation for the fraction of stars in the fainter RC is:

$$\begin{aligned}
 N_{\text{Faint}}/N_{\text{Total}} &= (0.402 \pm 0.055) + (-0.044 \pm 0.002) \times (l) \\
 &\quad + (-0.010 \pm 0.007) \times (|b| - 5), \\
 \delta &= 0.0047, \\
 \chi^2 &= 56.83, \\
 \text{DoF} &= 49.
 \end{aligned} \tag{18}$$

The scatter of $N_{\text{Faint}}/N_{\text{Total}}$ vs l is shown in Figure 10.

The reason for this correlation is that the Galactic bar's

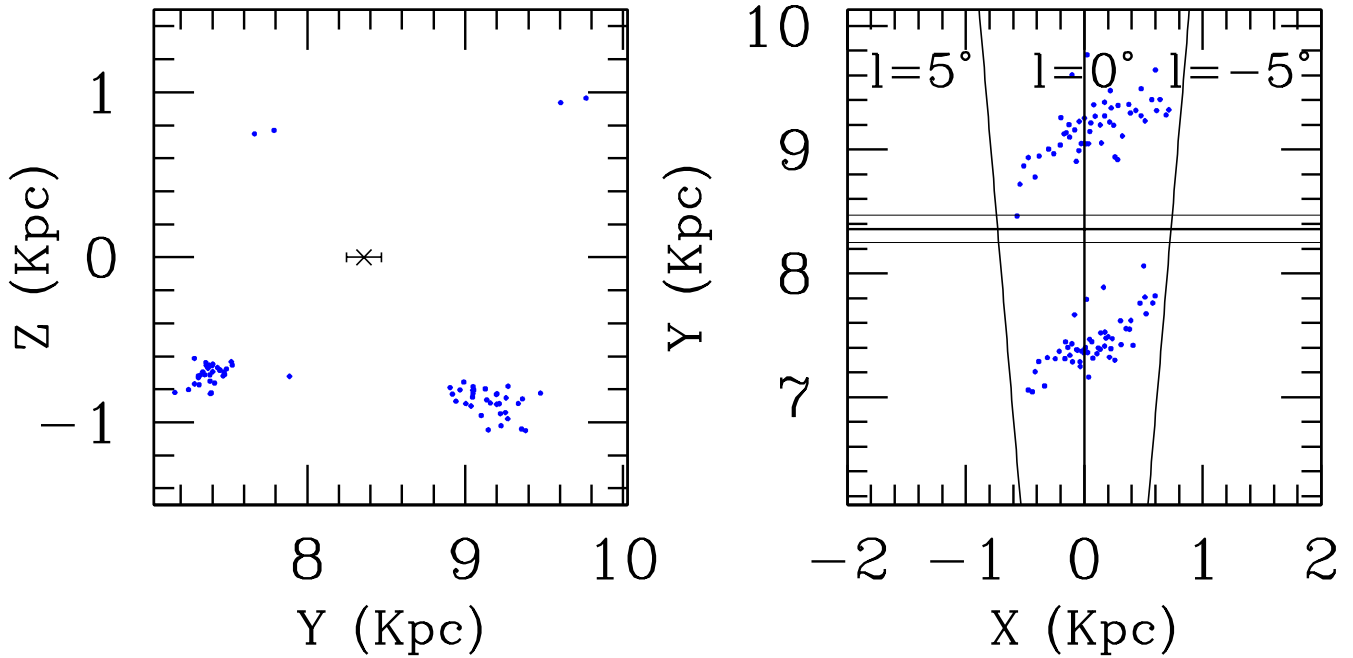


Figure 8. The mean positions of the observed red clump centroids in Galactic coordinate coordinates, where the Sun is located at $(X, Y, Z) = (0, 0, 0)$ and positive longitudes denote negative X-directions. The positions are derived by converting the mean brightness of the red clump into a distance by assuming an absolute magnitude of $M_{I,RC} = -0.12$. We show the estimated position of the Galactic centre with $1\text{-}\sigma$ error bars, (8.36 ± 0.11) Kpc, from Chatzopoulos et al. (2014), on both panels. : Projection of the red clump centroids onto the XZ plane, for measurements satisfying $-1^\circ \leq l \leq 1^\circ$. RIGHT: Projection of the RC centroids onto the XY plane.

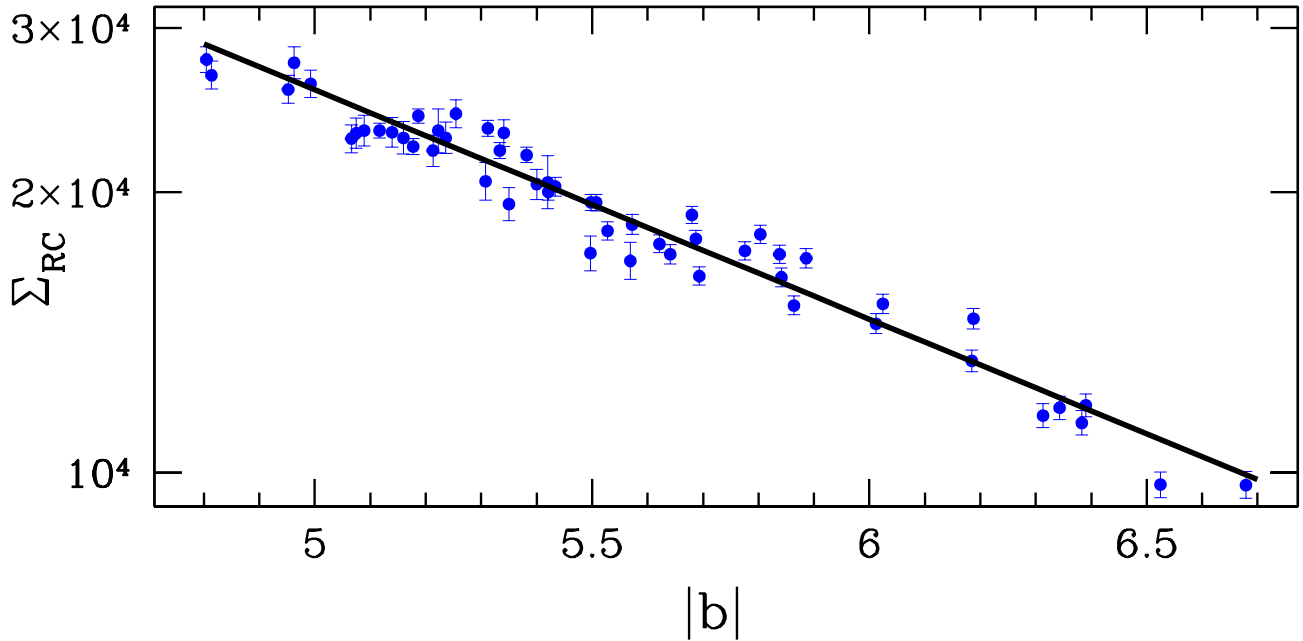


Figure 9. The surface density of red clump stars (in degrees^{-2}), Σ_{RC} , as a function of absolute latitude $|b|$. The data from individual fields are shown in blue, and the best-fit relation from Equation 17 is shown in black.

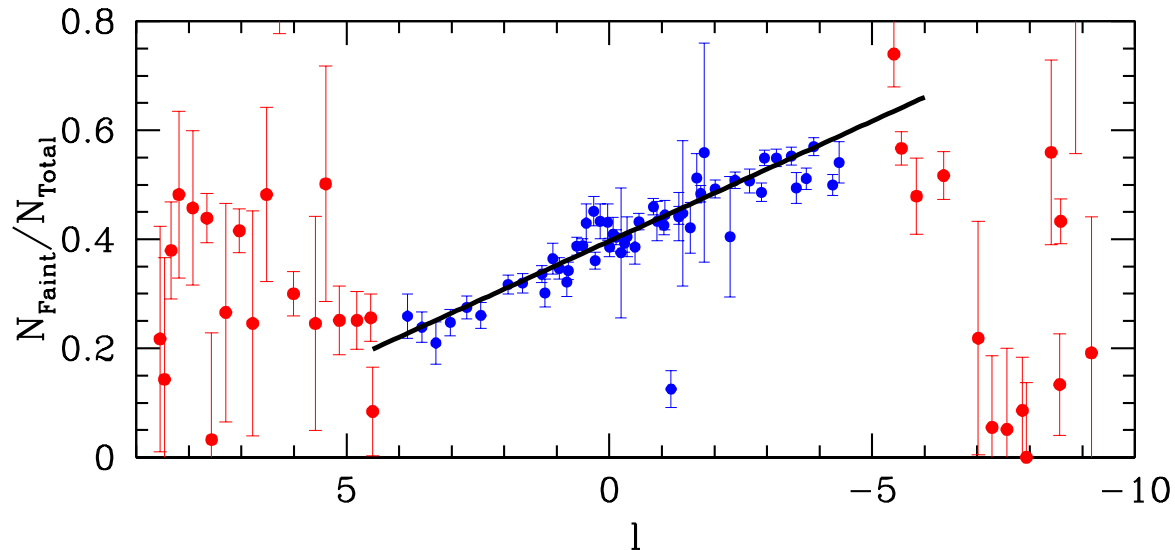


Figure 10. The fraction of red clump stars in the faint red clump, $N_{\text{Faint}}/N_{\text{Total}}$, is plotted as a function of Galactic longitude. The measurements for the calibration fields are shown in blue, and their best-fit relation is shown in black. The measurements for 33 additional fields are shown in red.

major axis is at an angle relative to the Sun-Galactic Centre line of sight (Stanek et al. 1997; Babusiaux & Gilmore 2005; Cao et al. 2013; Wegg & Gerhard 2013). If the arms of the X-shape protrude outward from the Galactic bar, it logically follows that the brighter RC should be relatively less numerous toward more negative longitudes, as the brighter RC would protrude from the nearer side of the bar. That the measurements become more erratic toward larger angular separations from the Galactic minor axis (red points, Figure 10) is possibly an indication of the “end” of the X-shape feature. N-body simulations consistently predict that the length of the peanut should be shorter than the total length of the bar closer to the plane (Athanasoula 2005), and this was specifically argued for our Galaxy by Martinez-Valpuesta & Gerhard (2011) and Romero-Gómez et al. (2011).

In Figure 11, we show the observed magnitude distribution of RC stars for five fields with varying longitude but nearly constant latitude. The fainter RC is virtually invisible toward $(l, b) = (3.30^\circ, -5.68^\circ)$ (field BLG 212) and becomes progressively clearer as longitude is decreased.

5.4 The Ratio of Red Clump Stars to Red Giant Stars

In Section 3.1, we defined EW_{RC} to be the ratio of the total number of RC stars to number density of RG stars per magnitude at the luminosity of the RC. We find that EW_{RC} is a slowly declining function of decreasing longitude and a steeply declining function of increasing absolute latitude (previously noted by Uttenthaler et al. 2012, see their Fig-

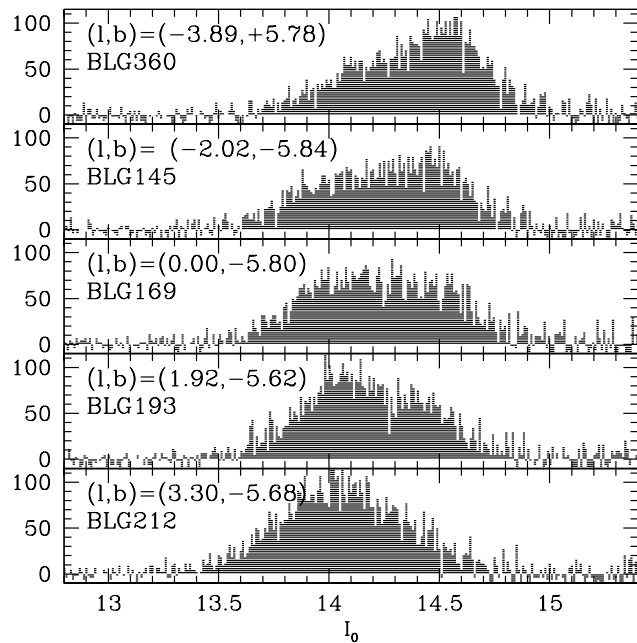


Figure 11. The fraction of RC stars in the faint-RC is a decreasing function of longitude. Shown are the dereddened magnitude histograms for five OGLE-III fields with the continuum fits to the RG+RGBB+AGBB removed from the observed number counts. Each histogram covers the same viewing area and is shown on the same scale. The best-fit ratio $N_{\text{Faint}}/N_{\text{Total}}$ progressively decreases from $(57 \pm 2)\%$ toward $(l, b) = (-3.89^\circ, +5.78^\circ)$ to $(21 \pm 4)\%$ toward $(l, b) = (3.30^\circ, -5.68^\circ)$. With the continuum RG+RGBB+AGB components to the luminosity function statistically subtracted, it is clear that the two peaks are slightly skew-symmetric.

ure 11 and related discussion):

$$\begin{aligned}
 EW_{RC} &= (1.213 \pm 0.010) + (0.007 \pm 0.002) \times (l) \\
 &\quad + (-0.164 \pm 0.013) \times (|b| - 5), \\
 \delta &= 0.0083, \\
 \chi^2 &= 78.01, \\
 \text{DoF} &= 50.
 \end{aligned} \tag{19}$$

The mean value is significantly below the intrinsic value of $EW_{RC} \approx 2.10$ (Nataf et al. 2014). At least a part of this is likely due to disk contamination: foreground RGs will have the same apparent magnitude as the RC if they are intrinsically fainter, which is where the luminosity function of RGs is highest. In contrast, the median value predicted by the convolution of the theoretical luminosity function with the N-body model is $EW_{RC} \approx 1.75$ for the models of Ness et al. (2012) and $EW_{RC} \approx 1.52$ for the model of Shen et al. (2010).

The solution to this discrepancy that we consider the likeliest is that the rate of disk contamination is higher than the rates of $\sim 6\%$ and $\sim 11\%$ predicted by the respective N-models of Ness et al. (2012) and Shen et al. (2010) – there is no reason to assume that the bulge-to-disk ratio in the model and their distributions along the line of sight would be the same as that for the Galaxy. A reduction from $EW_{RC} = 2.10$ to $EW_{RC} = 1.21$ (the value at $|b| = 5.0^\circ$) will occur if 19% of the stars near the luminosity of the RC are not bulge stars, and to $EW_{RC} = 0.97$ (the value at $|b| = 6.5^\circ$) will occur if 27% of the stars near the apparent magnitude of the RC are not bulge stars. These are compatible with the estimate of $\sim 25\%$ derived by Ness et al. (2013). Other possibilities include stellar models not correctly predicting the ratio of RC to RG stars, or that a significant fraction of bulge stars never go through the RC phase, see Calamida et al. (2014), who found that $\sim 30\%$ of white dwarfs being systematically cooler than canonical tracks.

6 DATA AND MODELS: A COMPARISON OF THREE OBSERVABLES

We compare the model predictions to the data for three observables, and for orientation angles $\alpha_{\text{Bar}} = 0, 15, 30, \text{ and } 45^\circ$. The central coordinates of the model prediction span longitudinal range $l = -10.5, -9.5, \dots +9.5$ and the latitudinal range $b = -5.5, -6.5$, with each point corresponding to a square with radius of length of 1 degree. The root-mean-square of the difference between the spline-interpolated model predictions and the observed parameters in the OGLE-III photometry are listed in Table 5.

The fraction of stars in the faint RC as a function of longitude (Figure 12) is predicted to show an increasing fraction towards decreasing longitudes, as expected, with the obvious exception of the case where the bar’s viewing angle is $\alpha_{\text{Bar}} = 0^\circ$. The cases $\alpha_{\text{Bar}} = 0, 15^\circ$ are the least consistent with the observations for both models. The model of Ness et al. (2012) is most consistent with the case $\alpha_{\text{Bar}} = 30^\circ$, whereas that of Shen et al. (2010) is comparably consistent with the cases $\alpha_{\text{Bar}} = 30, 45^\circ$ and nearly as consistent with the case $\alpha_{\text{Bar}} = 15^\circ$.

For the surface density of RC stars as a function of longitude (Figure 13), the data show an interesting feature: a

virtually flat surface density in the range $(-5.0^\circ \lesssim l \lesssim 4.0^\circ)$, with a steep log-linear dropoff outside of that range. We have found in our investigation that the combined surface density of RC stars is virtually insensitive to measurement systematics and degeneracies – the total RC+RGBB number density is a well-behaved observable with minimal uncertainties, and the only remaining degeneracies are how the relevant stars are partitioned into the different groups (bright vs faint RC, etc), not their total normalisation. Indeed, the top-left panel of Figure 21 of Nataf et al. (2013b), shows nearly the same profile for Σ_{RC} vs l in the case $|b| = 5.5^\circ$, even though those estimates were obtained using a single RC fit. We suggest that the fact the number density of stars falls off sharply beyond that longitudinal range may be an indicator of the length of the X-shape feature, at a height corresponding to $|b| \sim 5.5^\circ$. In other words, if we assume a Galactocentric distance $R_{GC} = 8.36$ Kpc and a viewing angle toward the bar of $\alpha_{\text{Bar}} = 30^\circ$, the drop off in density toward $(l, b) = (4^\circ, |5.5|^\circ)$ corresponds to a height of 0.72 Kpc from the Galactic plane at a distance of 1.04 Kpc from the Galactic centre. Conversely, the drop off in density toward $(l, b) = (-5^\circ, |5.5|^\circ)$ corresponds to a height of 0.95 Kpc from the Galactic plane at a distance of 1.72 Kpc from the Galactic centre. The first value is consistent with the location of the peak density at that separation from the plane inferred from Figure 19 of Wegg & Gerhard (2013), whereas the second value is $\sim 40\%$ further out, where the density is projected to have dropped closer to its value along the minor axis.

A peculiarity of this observable is that the predictions of both N-body models relative to the data show the the least integrated scatter for $\alpha_{\text{Bar}} = 0^\circ$. This orientation angle is already ruled out by various other arguments (Cao et al. 2013; Wegg & Gerhard 2013), and so this trend is unexpected. Inspection of Figure 13 shows that the discrepancy is largely due to predictions in the range $(-10.5^\circ \lesssim l \lesssim -5.0^\circ)$. Figure 13 makes clear that larger values of α_{Bar} would be favoured if the comparison were restricted to sightlines closer to the minor axis, which can also be found listed in Table 5, where we have included the scatter when restricting to sightlines that are closer to the minor axis.

The third observable investigated, that of $I_{RC, \text{Faint}} - I_{RC, \text{Bright}}$ as a function of longitude, has its observational and theoretical scatter vs longitude shown in Figure 14. As with the observable $N_{\text{Faint}}/N_{\text{Total}}$, the best match for the model of Ness et al. (2012) is for the case $\alpha_{\text{Bar}} = 30^\circ$, whereas the model of Shen et al. (2010) yields a comparably good match for the cases $\alpha_{\text{Bar}} = 30, 45^\circ$.

Table 5. Comparison of split red clump parameters in the OGLE-III photometry and in N-body model predictions. For each entry in the table we list the root-mean-square of the spline-interpolated model prediction and the observed value toward the sightline of the observation. The comparison for $N_{\text{Faint}}/N_{\text{Total}}$ and ΔI is for the 53 calibration fields that are not BLG 159A (an outlier in all aspects, see Table 3), and the comparison for Σ_{RC} is listed for both the sample of 53 sightlines and that of all 87 sightlines investigated in this work.

	$N_{\text{Faint}}/$ N_{Total}	$\Sigma_{RC,53}$	$\Sigma_{RC,87}$	ΔI
N12, $\alpha_{\text{Bar}} = 0^\circ$	0.11	0.12	0.12	0.08
N12, $\alpha_{\text{Bar}} = 15^\circ$	0.07	0.12	0.12	0.07
N12, $\alpha_{\text{Bar}} = 30^\circ$	0.05	0.11	0.13	0.04
N12, $\alpha_{\text{Bar}} = 45^\circ$	0.09	0.11	0.17	0.06
S10, $\alpha_{\text{Bar}} = 0^\circ$	0.09	0.12	0.13	0.10
S10, $\alpha_{\text{Bar}} = 15^\circ$	0.06	0.15	0.15	0.09
S10, $\alpha_{\text{Bar}} = 30^\circ$	0.05	0.11	0.15	0.05
S10, $\alpha_{\text{Bar}} = 45^\circ$	0.05	0.12	0.18	0.05

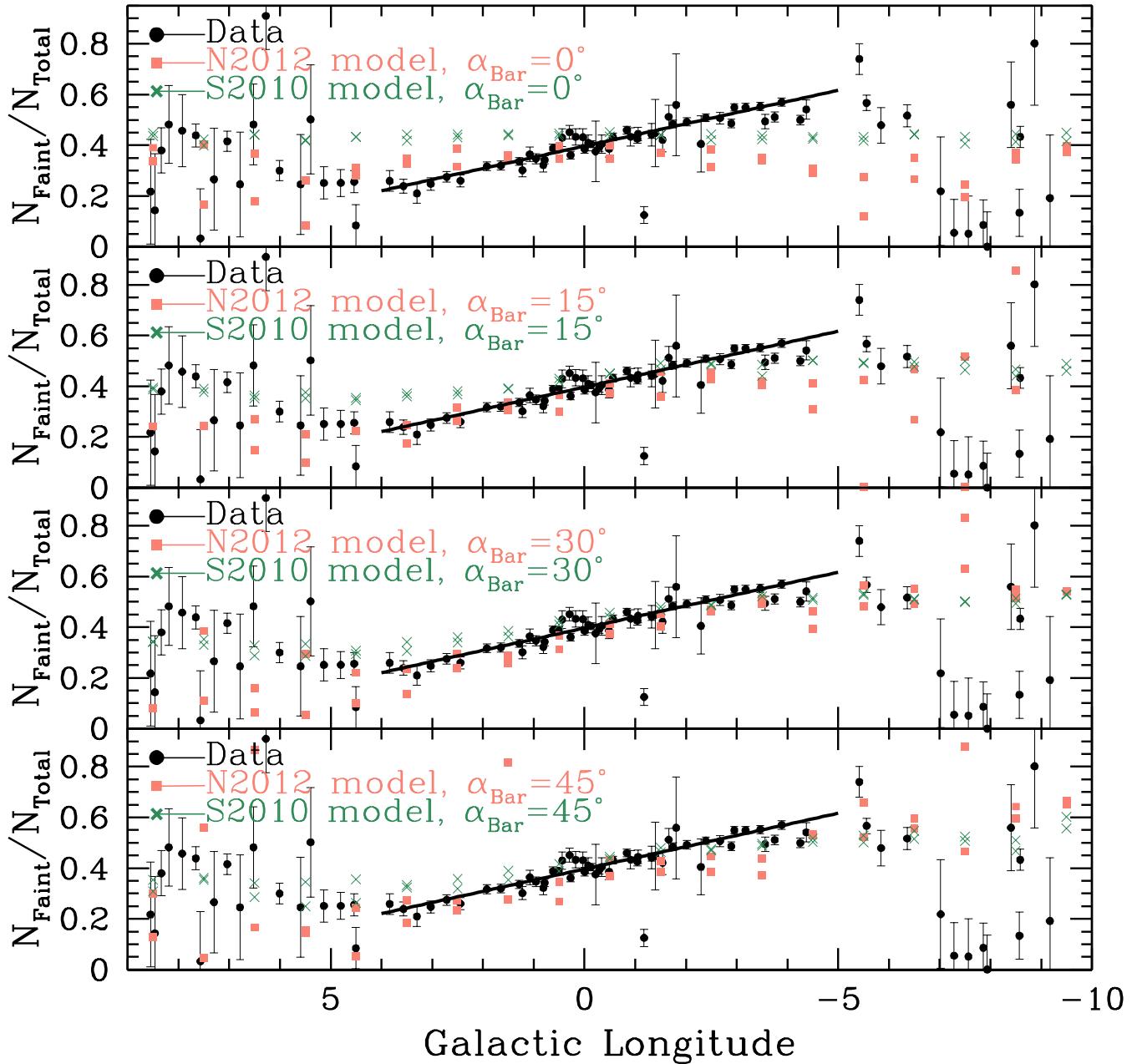


Figure 12. The fraction of red clump stars in the faint red clump as a function of longitude. Data points and best-fit relation are shown as black circles, predictions from the model are shown as salmon squares (Ness et al. 2012) and seagreen X's (Shen et al. 2010), for four different viewing angles to the Galactic bar, $\alpha_{\text{Bar}} = 0, 15, 30, 45^\circ$. The two predictions per N-body model per bin in longitude correspond to the $b = -5.5^\circ$ and $b = -6.5^\circ$ sightlines.

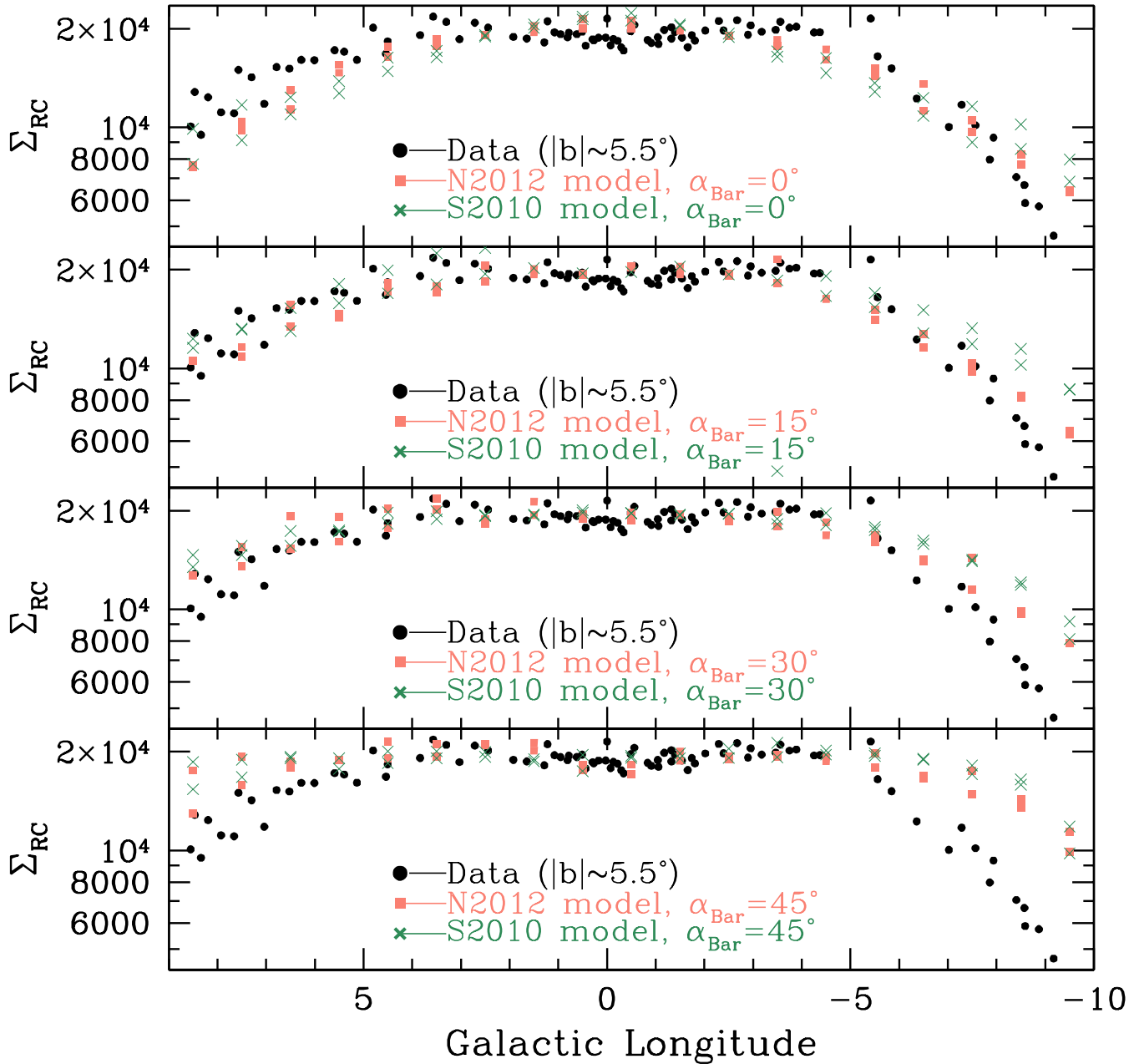


Figure 13. The surface density of red clump stars in degrees^{-2} as a function of longitude. Data points and best-fit relation are shown as black circles, which have been normalised to the value at $|b| = 5.5^\circ$ using Equation 17. Predictions from the model are shown as salmon squares (Ness et al. 2012) and seagreen X's (Shen et al. 2010), for four different viewing angles to the Galactic bar, $\alpha_{\text{Bar}} = 0, 15, 30, 45^\circ$. The two predictions per N-body model per bin in longitude correspond to the $b = -5.5^\circ$ and $b = -6.5^\circ$ sightlines.

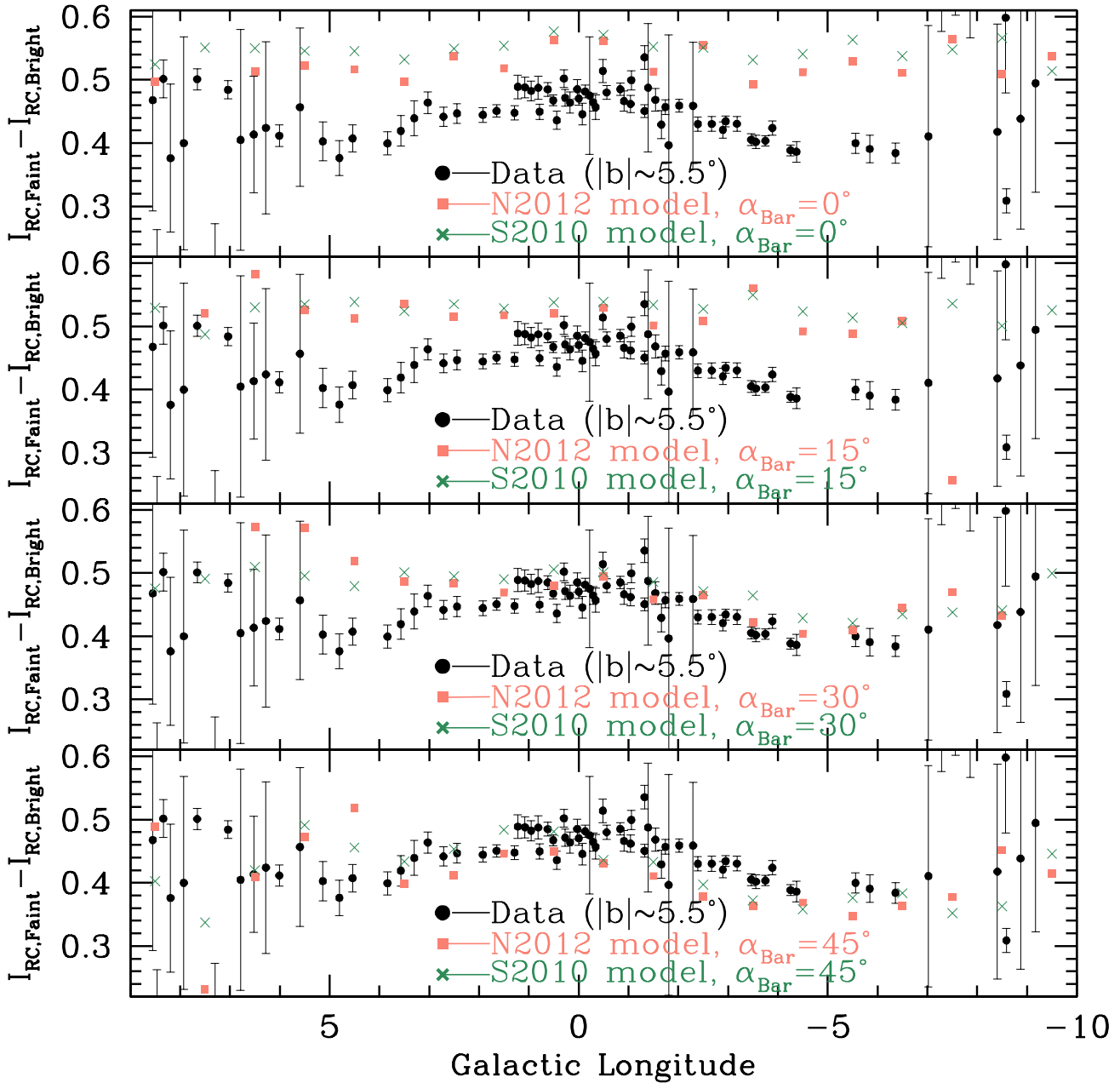


Figure 14. The brightness difference between the bright and faint red clump as a function of longitude. Data points and best-fit relation are shown as black circles, which have been normalised to the value at $|b| = 5.5^\circ$ using Equation 16. Predictions from the model are shown as salmon squares (Ness et al. 2012) and seagreen X's (Shen et al. 2010), for four different viewing angles to the Galactic bar, $\alpha_{\text{Bar}} = 0, 15, 30, 45^\circ$.

7 SUMMARY

In this investigation, we have made use of reddening maps from Nataf et al. (2013b) to precisely characterise the luminosity function of red giant stars toward the high-latitude fields, with the resulting RGBB parameters ($\Delta I_{RC}^{RC} = 0.61$, $f_{RC}^{RC} = 0.16$) being consistent with those measured closer to the plane ($\Delta I_{RC}^{RC} = 0.74$, $f_{RC}^{RC} = 0.20$) if one assumes a metallicity difference of $\Delta[M/H] \approx 0.22$ dex. The exponential slope of the RG luminosity function continuum can be fixed to $B = 0.578$, at least for the directions probed in this work. The magnitude dispersion of the RC toward these sightlines (typically ~ 0.22 mag for the brighter RC) is dominated by geometric dispersion, as evidenced by the fact that the ratio $\sigma_{RC,2}/\sigma_{RC,1} = 0.80$ can be explained purely by geometry. We have also found that for these sightlines, skew-Gaussians with $\alpha_{\text{skew}} = -1.50$ for the brighter RC and $\alpha_{\text{skew}} = +1.50$ for the fainter RC yield a superior fit to the luminosity function than standard Gaussians.

The ratio of RC stars to RG stars is found to be much lower than predicted from stellar theory. We measure $EW_{RC} \approx 1.21 - 0.164 * (|b| - 5)$. This can be reconciled with theory if 19% and 27% of stars near the brightness and colour of the RC are disk contaminants toward $|b| = 5^\circ$ and $|b| = 6.5^\circ$, respectively, similar to the estimate of $\sim 25\%$ derived by Ness et al. (2013). Alternatively, there may be a significant fraction of bulge stars in close binaries that lose extra mass as they ascend the RGB and thus never begin the core-helium-burning phase, as recently suggested by Calamida et al. (2014).

The precise luminosity function and reddening maps allow us to map the directional-dependence of the brightness of the brighter RC, the brightness separation between the two RCs, the total surface density of RC stars on the sky, and the fraction of stars in the brighter RC. All of the observables show smooth behaviour toward ($-5.0^\circ \lesssim l \lesssim 4.0^\circ$). Outside of that range, most observables yield erratic measurements. A notable exception being that of the total surface density of RC stars Σ_{RC} , an observable that is relatively impervious to systematic measurement errors. It falls off smoothly and rapidly outside that range.

In our comparison to N-body models, we have found that the case where the orientation angle $\alpha_{\text{Bar}} = 30^\circ$ is favoured by the model of Ness et al. (2012) whereas $\alpha_{\text{Bar}} = 30, 45^\circ$ are comparably favoured by the models of Shen et al. (2010). As is expected, no perfect match is to be found. The biggest discrepancies between models and data are in the rate of decline of the combined surface density of red clump stars toward negative longitudes and of the brightness difference between the two RCs toward positive longitudes.

The two models tested are, perhaps surprisingly, more distinct from the data as they are from one another in their predictions. Though some progress has been made in the literature in recent years in comparing observational data of the Galactic bulge to N-body models (Shen et al. 2010; Martinez-Valpuesta & Gerhard 2011; Li et al. 2014; Li & Shen 2012; Ness et al. 2012; Vásquez et al. 2013; Ness et al. 2013; Gardner et al. 2014), these discrepancies demonstrate that there remain significant issues to resolve, significant diversity in the allowed kinematic parameter space. We note that all models are internally-consistent dynamical pictures of what a galaxy could conceivably look

like, but there are countless variables from the mass ratios of the different components to their initial angular momenta to the shape of the dark matter halo – it would nearly be a miracle to achieve a perfect match to the Milky Way, which is one specific galaxy with its own distinct assembly history, in addition to possible undiagnosed systematics arising from the convolving of isochrones with N-body models to simulate how the data is observed. We have also not accounted for possible variations due to correlations between kinematics and chemistry, which are significant for the bulge stellar population (Zoccali et al. 2008; Babusiaux et al. 2010; Ness et al. 2012, 2013; Babusiaux et al. 2014) and could distort the resulting luminosity function and interpretations thereof (Nataf et al. 2014). Nevertheless, the Milky Way remains the only Galaxy that we can study in all six dimensions of kinematic phase space (plus chemistry) with great precisions, thus justifying attempts to delineate and decipher as many morphological components as accurately as possible, with corresponding explanation in theoretically-understood dynamical phenomena.

8 ACKNOWLEDGMENTS

We thank Andrew Gould and Martin Asplund for helpful discussions. We thank the referee for a helpful report that improved the manuscript.

DMN was primarily supported by the Australian Research Council grant FL110100012, and partially supported by the NSERC grant PGSD3-403304-2011 and the NSF grant AST-1103471. EA acknowledges financial support from the CNES (Centre National d'Etudes Spatiales - France) and from the People Programme (Marie Curie Actions) of the European Union's Seventh Framework Programme FP7/2007-2013/ under REA grant agreement number PITN-GA-2011-289313 to the DAGAL network. EA is thankful for HPC resources from GENCI- TGCC/CINES (Grants 2013 - x2013047098 and 2014 - x2014047098). JS acknowledges the support from the 973 Program of China under grants No. 2014CB845701, the National Natural Science Foundation of China under grants No. 11073037, 11333003, 11322326, and the Strategic Priority Research Program "The Emergence of Cosmological Structures" (No. XDB09000000) of Chinese Academy of Sciences. ZYL is grateful for the support from Shanghai Yangfan Talent Youth Program (No. 14YF1407700).

The OGLE project has received funding from the European Research Council under the European Community's Seventh Framework Programme (FP7/2007-2013) / ERC grant agreement no. 246678 to AU.

This work has made use of BaSTI web tools.

REFERENCES

- Athanassoula, E. 2003, MNRAS, 341, 1179
- Athanassoula, E. 2005, MNRAS, 358, 1477
- Babusiaux, C., & Gilmore, G. 2005, MNRAS, 358, 1309
- Babusiaux, C., Gómez, A., Hill, V., et al. 2010, A&A, 519, A77
- Babusiaux, C., Katz, D., Hill, V., et al. 2014, A&A, 563, A15

- Bjork, S. R., & Chaboyer, B. 2006, *ApJ*, 641, 1102
- Bureau, M., Aronica, G., Athanassoula, E., et al. 2006, *MNRAS*, 370, 753
- Cassisi, S., & Salaris, M. 1997, *MNRAS*, 285, 593
- Calamida, A., Sahu, K. C., Anderson, J., et al. 2014, arXiv:1406.6451
- Cao, L., Mao, S., Nataf, D., Rattenbury, N. J., & Gould, A. 2013, *MNRAS*, 434, 595
- Chatzopoulos, S., Fritz, T., Gerhard, O., et al. 2014, arXiv:1403.5266
- Cordier D., Pietrinferni A., Cassisi S., Salaris M., 2007, *AJ*, 133, 468
- Dwek, E., Arendt, R. G., Hauser, M. G., et al. 1995, *ApJ*, 445, 716
- Freeman, K., Ness, M., Wylie-de-Boer, E., et al. 2013, *MNRAS*, 428, 3660
- Gardner, E., Debattista, V. P., Robin, A. C., Vásquez, S., & Zoccali, M. 2014, *MNRAS*, 438, 3275
- Gillessen, S., Eisenhauer, F., Trippe, S., et al. 2009, *ApJ*, 692, 1075
- Gonzalez, O. A., Rejkuba, M., Zoccali, M., et al. 2012, *A&A*, 543, A13
- Howard, C. D., Rich, R. M., Reitzel, D. B., et al. 2008, *ApJ*, 688, 1060
- Kunder, A., Koch, A., Rich, R. M., et al. 2012, *AJ*, 143, 57
- Laurikainen, E., Salo, H., Athanassoula, E., et al. 2013, *MNRAS*, 430, 3489
- Laurikainen, E., Salo, H., Athanassoula, E., Bosma, A., & Herrera-Endoqui, M. 2014, arXiv:1406.1418
- Li, Z.-Y., & Shen, J. 2012, *ApJ*, 757, L7
- Li, Z.-Y., Shen, J., Rich, R. M., Kunder, A., & Mao, S. 2014, *ApJ*, 785, L17
- Martinez-Valpuesta, I., & Gerhard, O. 2011, *ApJ*, 734, L20
- McWilliam, A., & Zoccali, M. 2010, *ApJ*, 724, 1491
- Nataf, D. M., Udalski, A., Gould, A., Fouqué, P., & Stanek, K. Z. 2010, *ApJ*, 721, L28
- Nataf, D. M., Udalski, A., Gould, A., & Pinsonneault, M. H. 2011, *ApJ*, 730, 118
- Nataf, D. M., Gould, A. P., Pinsonneault, M. H., & Udalski, A. 2013a, *ApJ*, 766, 77
- Nataf, D. M., Gould, A., Fouqué, P., et al. 2013b, *ApJ*, 769, 88
- Nataf, D. M., Cassisi, S., & Athanassoula, E. 2014, *MNRAS*, 442, 2075
- Ness, M., Freeman, K., Athanassoula, E., et al. 2012, *ApJ*, 756, 22
- Ness, M., Freeman, K., Athanassoula, E., et al. 2013, *MNRAS*, 430, 836
- Ness, M., Freeman, K., Athanassoula, E., et al. 2013, *MNRAS*, 432, 2092
- Patsis, P. A., Skokos, C., & Athanassoula, E. 2002, *MNRAS*, 337, 578
- Pietrinferni, A., Cassisi, S., Salaris, M., & Castelli, F. 2004, *ApJ*, 612, 168
- Poleski, R., Udalski, A., Gould, A., et al. 2013, *ApJ*, 776, 76
- Romero-Gómez, M., Athanassoula, E., Antoja, T., & Figueras, F. 2011, *MNRAS*, 418, 1176
- Salaris, M., & Girardi, L. 2002, *MNRAS*, 337, 332
- Saito, R. K., Hempel, M., Minniti, D., et al. 2012, *A&A*, 537, A107
- Salpeter, E. E. 1955, *ApJ*, 121, 161
- Schönrich, R. 2012, *MNRAS*, 427, 274
- Shen, J., Rich, R. M., Kormendy, J., et al. 2010, *ApJ*, 720, L72
- Shen, J. 2014, *IAU Symposium*, 298, 201
- Skokos, C., Patsis, P. A., & Athanassoula, E. 2002, *MNRAS*, 333, 861
- Skrutskie, M. F., Cutri, R. M., Stiening, R., et al. 2006, *AJ*, 131, 1163
- Stanek, K. Z., Mateo, M., Udalski, A., et al. 1994, *ApJ*, 429, L73
- Stanek, K. Z., Udalski, A., Szymański, M., et al. 1997, *ApJ*, 477, 163
- Szymański, M. K., Udalski, A., Soszyński, I., et al. 2011, *Acta Astronom.*, 61, 83
- Udalski, A., Szymanski, M., Kubiak, M., et al. 2002, *Acta Astronom.*, 52, 217
- Udalski, A. 2003, *Acta Astronomica*, 53, 291
- Udalski, A., Szymański, M. K., Soszyński, I., & Poleski, R. 2008, *Acta Astronomica*, 58, 69
- Uttenthaler, S., Schultheis, M., Nataf, D. M., et al. 2012, *A&A*, 546, A57
- Vásquez, S., Zoccali, M., Hill, V., et al. 2013, *A&A*, 555, A91
- Wegg, C., & Gerhard, O. 2013, *MNRAS*, 435, 1874
- Zoccali, M., Hill, V., Lecureur, A., et al. 2008, *A&A*, 486, 177